

NASA Technical Memorandum 103099  
ICOMP-90-13

# Implicit Solution of Three-Dimensional Internal Turbulent Flows

V. Michelassi  
*Institute for Computational Mechanics in Propulsion*  
*Lewis Research Center*  
*Cleveland, Ohio*

M.-S. Liou and L.A. Povinelli  
*Lewis Research Center*  
*Cleveland, Ohio*

(NASA-TM-103099) IMPLICIT SOLUTION OF  
THREE-DIMENSIONAL INTERNAL TURBULENT FLOWS  
(NASA) 45 0 CSCL 200

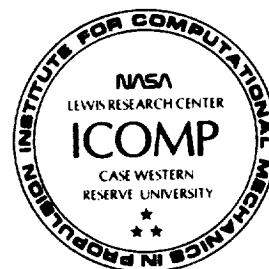
NPO-27982

Unclass

41/34 0302649

July 1990

**NASA**





# Implicit Solution of Three-Dimensional Internal Turbulent Flows

V. Michelassi\*

Institute for Computational Mechanics in Propulsion  
Lewis Research Center  
Cleveland, Ohio 44135

M.-S. Liou and L. A. Povinelli

National Aeronautics and Space Administration  
Lewis Research Center  
Cleveland, Ohio 44135

## Summary

The scalar form of the approximate factorization method has been used to develop a new code for the solution of three-dimensional internal laminar and turbulent compressible flows. The Navier-Stokes equations in their Reynolds-averaged form are iterated in time until a steady solution is reached. Evidence is given to the implicit and explicit artificial damping schemes that proved to be particularly efficient in speeding up convergence and enhancing the algorithm robustness. A conservative treatment of these terms at domain boundaries is proposed in order to avoid undesired mass and/or momentum artificial fluxes. Turbulence effects are accounted for by the zero-equation Baldwin-Lomax turbulence model and the  $q-\omega$  two-equation model. For the first, an investigation on the model behavior in the case of multiple boundaries is performed. The flow in a developing S-duct is then solved in the laminar regime at Reynolds number (Re) 790 and in the turbulent regime at  $Re=40,000$  using the Baldwin-Lomax model. The Stanitz elbow is then solved by using an inviscid version of the same code at  $M_{inlet}=0.4$ . Grid dependence and convergence rate are investigated showing that for this solver the implicit damping scheme may play a critical role for convergence characteristics. The same flow at  $Re=2.5 \cdot 10^6$  is solved with the Baldwin-Lomax and the  $q-\omega$  models. Both approaches show satisfactory agreement with experiments, although the  $q-\omega$  model is slightly more accurate.

## Chapter 1

### INTRODUCTION

With the advent of more and more powerful supercomputers, the numerical solution of three-dimensional turbulent flows has become possible (ref. 1). Although it is well known that lower order turbulence closures fail to reproduce secondary motions of Prandtl's second kind (turbulence driven), they normally succeed in predicting secondary flows of the first kind (pressure

\* Work funded under Space Act Agreement C-99066-G; on leave from the University of Florence, Italy.

driven). Therefore, for many complex configurations it has been possible to obtain fairly accurate results with zero and two-equation turbulence models (ref. 2) with a reasonable prediction of pressure-driven secondary flows.

For three-dimensional blade-passage flows, a correct prediction of the wake behavior has been obtained by Yokota (ref. 3) by means of the standard high-Reynolds-number form of the  $k-\epsilon$  two-equation model with the wall function approach. However the zero-equation model implemented in reference 3 did not give a satisfactory depiction of the flow in the wake region. For the prediction of blade pressure distribution, the Baldwin-Lomax (ref. 4) zero-equation turbulence model was found to give accurate results in several flow configurations (ref. 5) despite the low convergence rate. For incompressible internal flows with no separation, good results have been obtained by Towne (ref. 6) with a zero-equation turbulence model and a parabolized Navier-Stokes solver. Still, for practical flow configurations, it is necessary to face quite long computing times mainly because of the large number of points usually required for a detailed description of the flow field. Moreover, the non-linearities associated with nearly all the turbulence models can play a significant role in slowing down the convergence rate to the steady state solution. This behavior is independent of the implicit or explicit nature of the flow solver and is intrinsic to the turbulence models (zero- or two-equation.)

In two dimensions, a wide variety of flow conditions have been accurately solved by means of low-Reynolds-number forms of the  $k-\epsilon$  model in which the effect of laminar viscosity is explicitly accounted for (see refs. 7-9). In nearly all the flow conditions investigated, these forms proved to be more accurate than the standard high-Re formulation, provided that a sufficient number of grid points are located inside the viscous and buffer layers; in fact, secondary motions and losses are mainly driven by what happens close to walls so that a correct description of this flow region is crucial for an accurate simulation of the flow pattern. Rodi (ref. 9) found that the use of the low-Reynolds-number forms of the  $k-\epsilon$  model could give the prediction of secondary flows normally lost with the high-Reynolds-number form. Unfortunately, the first author (ref. 7), found some of these forms extremely stiff from a numerical point of view. The stiffness was mainly caused by the low-Reynolds-number effect terms in which exponential functions are introduced to model the wall effects. From this standpoint, it appeared worthwhile investigating some features of the turbulence model for internal turbulent flows by using an implicit algorithm. Since complex flow patterns, such as separation and dominant viscous effects, are expected in internal flows, the implicit approach was selected to increase the robustness and convergence rate of the numerical procedure when zero- and two-equation turbulence models were used.

## Chapter 2

## DESCRIPTION OF THE ALGORITHM

### 2.1 - Navier-Stokes Equations

The Boussinesq hypothesis allows relating the turbulent shear stresses to the mean strains via the so-called "eddy viscosity" so that, under this assumption, the three-dimensional Reynolds-averaged Navier-Stokes (N-S) equations can be written in divergence form and,

subsequently, transformed from the Cartesian coordinate system  $(x,y,z)$  to the generalized curvilinear coordinate system  $\xi,\eta,\zeta$ . The resulting set of equations can be written in vector form as follows:

$$\frac{\partial \bar{Q}}{\partial t} + \frac{\partial \bar{E}}{\partial \xi} + \frac{\partial \bar{F}}{\partial \eta} + \frac{\partial \bar{G}}{\partial \zeta} = \frac{\partial \bar{E}_v}{\partial \xi} + \frac{\partial \bar{F}_v}{\partial \eta} + \frac{\partial \bar{G}_v}{\partial \zeta} \quad (2.1)$$

where the flux vectors are

$$\bar{Q} = J^{-1} \begin{bmatrix} \rho \\ \rho U \\ \rho V \\ \rho W \\ e \end{bmatrix}$$

$$\bar{E} = J^{-1} \begin{bmatrix} \rho U \\ \rho U U + \xi_x p \\ \rho V U + \xi_y p \\ \rho W U + \xi_z p \\ U(e+p) \end{bmatrix}$$

$$\bar{F} = J^{-1} \begin{bmatrix} \rho V \\ \rho U V + \eta_x p \\ \rho V V + \eta_y p \\ \rho W V + \eta_z p \\ V(e+p) \end{bmatrix}$$

$$\bar{G} = J^{-1} \begin{bmatrix} \rho W \\ \rho U W + \zeta_x p \\ \rho V W + \zeta_y p \\ \rho W W + \zeta_z p \\ W(e+p) \end{bmatrix}$$

$$\bar{E}_v = \frac{J^{-1}}{Re} \begin{bmatrix} 0 \\ \zeta_x \tau_{xx} + \zeta_y \tau_{xy} + \zeta_z \tau_{xz} \\ \zeta_x \tau_{xy} + \zeta_y \tau_{yy} + \zeta_z \tau_{yz} \\ \zeta_x \tau_{xz} + \zeta_y \tau_{yz} + \zeta_z \tau_{zz} \\ \zeta_x E_e + \zeta_y F_e + \zeta_z G_e \end{bmatrix}$$

$$\bar{F}_v = \frac{J^{-1}}{Re} \begin{bmatrix} 0 \\ \eta_x \tau_{xx} + \eta_y \tau_{xy} + \eta_z \tau_{xz} \\ \eta_x \tau_{xy} + \eta_y \tau_{yy} + \eta_z \tau_{yz} \\ \eta_x \tau_{xz} + \eta_y \tau_{yz} + \eta_z \tau_{zz} \\ \eta_x E_e + \eta_y F_e + \eta_z G_e \end{bmatrix}$$

$$\bar{G}_v = \frac{J^{-1}}{Re} \begin{bmatrix} 0 \\ \zeta_x \tau_{xx} + \zeta_y \tau_{xy} + \zeta_z \tau_{xz} \\ \zeta_x \tau_{xy} + \zeta_y \tau_{yy} + \zeta_z \tau_{yz} \\ \zeta_x \tau_{xz} + \zeta_y \tau_{yz} + \zeta_z \tau_{zz} \\ \zeta_x E_e + \zeta_y F_e + \zeta_z G_e \end{bmatrix}$$

$U$ ,  $V$ ,  $W$  are the unscaled contravariant velocities defined as follows:

$$U = \xi_x U + \xi_y V + \xi_z W$$

$$V = \eta_x U + \eta_y V + \eta_z W$$

$$W = \zeta_x U + \zeta_y V + \zeta_z W$$

The shear stresses in three dimensions are

$$\tau_{xx} = \mu_{\text{eff}} \left( \frac{4}{3} \frac{\partial U}{\partial x} - \frac{2}{3} \left( \frac{\partial V}{\partial y} + \frac{\partial W}{\partial z} \right) \right)$$

$$\tau_{yy} = \mu_{\text{eff}} \left( \frac{4}{3} \frac{\partial V}{\partial y} - \frac{2}{3} \left( \frac{\partial U}{\partial x} + \frac{\partial W}{\partial z} \right) \right)$$

$$\tau_{zz} = \mu_{\text{eff}} \left( \frac{4}{3} \frac{\partial W}{\partial z} - \frac{2}{3} \left( \frac{\partial U}{\partial x} + \frac{\partial V}{\partial y} \right) \right)$$

$$\tau_{xy} = \tau_{yx} = \mu_{\text{eff}} \left( \frac{\partial U}{\partial y} + \frac{\partial V}{\partial x} \right)$$

$$\tau_{xz} = \tau_{zx} = \mu_{\text{eff}} \left( \frac{\partial U}{\partial z} + \frac{\partial W}{\partial x} \right)$$

$$\tau_{yz} = \tau_{zy} = \mu_{\text{eff}} \left( \frac{\partial V}{\partial z} + \frac{\partial W}{\partial y} \right)$$

and

$$E_e = U \tau_{xx} + V \tau_{xy} + W \tau_{xz} + \mu_e \frac{1}{(\gamma-1)} \frac{\partial a^2}{\partial x}$$

$$F_e = U \tau_{yx} + V \tau_{yy} + W \tau_{yz} + \mu_e \frac{1}{(\gamma-1)} \frac{\partial a^2}{\partial y}$$

$$G_e = U \tau_{zx} + V \tau_{zy} + W \tau_{zz} + \mu_e \frac{1}{(\gamma-1)} \frac{\partial a^2}{\partial z}$$

in which the following definition for the  $x$ , as well as for  $y$  and  $z$  Cartesian derivatives, holds:

$$\frac{\partial}{\partial x} = \xi_x \frac{\partial}{\partial \xi} + \eta_x \frac{\partial}{\partial \eta} + \zeta_x \frac{\partial}{\partial \zeta}$$

In this set of equations,  $\rho$  is the fluid density,  $p$  is the static pressure,  $e$  is the total energy per unit volume,  $a$  is the sound speed, and  $(U, V, W)$  are the Cartesian components of the velocity vector. According to the Boussinesq assumption, the diffusion coefficients for momentum and energy are defined as follows

$$\mu_{\text{eff}} = \mu_l + \mu_t \quad \text{and} \quad \mu_h = \frac{\mu_l}{Pr_l} + \frac{\mu_t}{Pr_t}$$

in which  $\mu_l$  is the laminar viscosity that was considered independent of the static temperature, and  $\mu_t$  is the turbulent viscosity obtained from the turbulence model. In this set of calculations, the turbulent Prandtl number  $Pr_t$  was set equal to 0.90 and the laminar Prandtl number  $Pr_l$  was 0.72. The relation between static pressure and total energy is obtained through the equation of state for a perfect gas that yields

$$p = (\gamma - 1) \left( e - \rho \frac{U^2 + V^2 + W^2}{2} \right)$$

in which  $\gamma = 1.4$  is the ratio of specific heat capacities for air.

### 2.1.1 - Metric relations

The metrics are usually obtained from a chain rule expansion of  $x_\xi, x_\eta, x_\zeta, y_\xi, y_\eta, y_\zeta, z_\xi, z_\eta, z_\zeta$ . The following definitions of the metric relations hold:

$$\begin{aligned} \xi_x &= J(y_\eta z_\zeta - y_\zeta z_\eta) ; \quad \xi_y = J(z_\eta x_\zeta - z_\zeta x_\eta) ; \quad \xi_z = J(y_\zeta x_\eta - y_\eta x_\zeta) \\ \eta_x &= J(z_\xi y_\zeta - y_\zeta z_\xi) ; \quad \eta_y = J(x_\xi z_\zeta - x_\zeta z_\xi) ; \quad \eta_z = J(y_\xi x_\zeta - y_\zeta x_\xi) \\ \zeta_x &= J(y_\xi z_\eta - z_\eta y_\xi) ; \quad \zeta_y = J(x_\eta z_\xi - x_\xi z_\eta) ; \quad \zeta_z = J(x_\xi y_\eta - y_\eta x_\xi) \end{aligned}$$

and the jacobian of the coordinate transformation is given by

$$J^{-1} = x_\xi y_\eta z_\zeta + x_\zeta y_\xi z_\eta + x_\eta y_\zeta z_\xi - x_\xi y_\zeta z_\eta - x_\eta y_\xi z_\zeta - x_\zeta y_\eta z_\xi$$

The flux vectors are discretized by using centered finite differences. When the centered discretization is used for the metrics, it can be shown that in three dimensions the metric invariants are not satisfied (ref. 10). This may result in large discretization error. However, it is possible to satisfy the invariants by a simple averaging technique that gives metrics similar to those computed by a finite volume method. For example,  $\xi_x$  is computed as

$$\xi_x = J \left( \chi_\zeta \left( \frac{\partial y}{\partial \eta} \right) \chi_\eta \left( \frac{\partial z}{\partial \zeta} \right) - \chi_\eta \left( \frac{\partial y}{\partial \zeta} \right) \chi_\zeta \left( \frac{\partial z}{\partial \eta} \right) \right)$$

in which  $\chi$  is a central average operator. This averaging process was found to ensure better mass conservation properties in the present calculations, especially for highly stretched grids.

### 2.1.2 - Nondimensionalization

Since the solver is specifically designed to compute internal flows, the set of equations is nondimensionalized with respect to the total quantities in the inlet section, indicated with



subscript 01.

$$\bar{U} = \frac{U}{\sqrt{a_{01}^2/\gamma}} ; \bar{V} = \frac{V}{\sqrt{a_{01}^2/\gamma}} ; \bar{W} = \frac{W}{\sqrt{a_{01}^2/\gamma}} ; \bar{a} = \frac{a}{\sqrt{a_{01}^2/\gamma}}$$

$$\bar{e} = \frac{e}{a_{01}^2/\gamma} ; \bar{\rho} = \frac{\rho}{\rho_{01}} ; \bar{p} = \frac{p}{p_{01}} ; \bar{\mu} = \frac{\mu}{\mu_1}$$

Following this nondimensionalization, the flow Reynolds number (Re) is defined as

$$Re = \frac{\sqrt{(RT_{01})} \rho_{01} L}{\mu}$$

in which L is typically a characteristic dimension of the inlet section.

## 2.2 - Approximate Factorization; Scalar Form

The approximate factorization method first proposed by Beam and Warming (ref. 11) splits an n-dimensional operator into the product of n one-dimensional operators. This technique provides a strong link between the equations insofar as they are solved fully coupled. The main drawback to this method lies in the necessity of time-consuming block tri- or pentadiagonal matrix inversion. This problem becomes more evident in three dimensions where the coupled solution yields a 5x5 block tridiagonal matrix. In order to make this algorithm more efficient and still maintain its strong implicit nature, Pulliam (refs. 10 and 12) proposed a scalar form of the approximate factorization. The form of the standard algorithm in three dimensions can be written as follows:

$$[I + \theta \Delta t (\delta_\xi A - \delta_\xi^2 A_v)] * [I + \theta \Delta t (\delta_\eta B - \delta_\eta^2 B_v)] * [I + \theta \Delta t (\delta_\zeta C - \delta_\zeta^2 C_v)] * \Delta Q = \text{RHS} \quad (2.2)$$

in which I is the identity matrix,  $\theta$  is a parameter that allows weighting the explicit-implicit nature of the space operator (in the present calculations, since the steady state solution was sought,  $\theta=1$  was used that gave first-order accuracy in time),  $\delta$  is a centered difference operator,  $\Delta t$  is the time step,  $\Delta Q = Q^{n+1} - Q^n$ , and  $Q = J \bar{Q}$ . The convective jacobians are A, B and C;  $A_v$ ,  $B_v$ , and  $C_v$  are the diffusive jacobians in the three directions  $\xi$ ,  $\eta$ ,  $\zeta$ ; and RHS represents the convective and diffusive fluxes defined as follows:

$$A = \frac{\partial \bar{E}}{\partial \bar{Q}} ; B = \frac{\partial \bar{F}}{\partial \bar{Q}} ; C = \frac{\partial \bar{G}}{\partial \bar{Q}}$$

$$A_v = \frac{\partial \bar{E}_v}{\partial \bar{Q}} ; B_v = \frac{\partial \bar{F}_v}{\partial \bar{Q}} ; C_v = \frac{\partial \bar{G}_v}{\partial \bar{Q}}$$

$$\text{RHS} = \Delta t \left( -\frac{\partial \bar{E}}{\partial \xi} - \frac{\partial \bar{F}}{\partial \eta} - \frac{\partial \bar{G}}{\partial \zeta} + \frac{\partial \bar{E}_v}{\partial \xi} + \frac{\partial \bar{F}_v}{\partial \eta} + \frac{\partial \bar{G}_v}{\partial \zeta} \right)$$

The jacobian matrices A, B, C, A<sub>v</sub>, B<sub>v</sub>, and C<sub>v</sub>, that can be found in Pulliam (ref. 10) are full and require a general inversion process. Pulliam and Chaussee (ref. 12) proposed a more efficient procedure by making some simplifications. First, the hyperbolic property of the convective jacobians allows the diagonalization as

$$A = T_\xi \Lambda_\xi T_\xi^{-1}; \quad B = T_\eta \Lambda_\eta T_\eta^{-1}; \quad C = T_\zeta \Lambda_\zeta T_\zeta^{-1} \quad (2.3)$$

in which T represents the eigenvector matrices, defined in (ref. 12). The eigenvalues of the jacobians in three dimensions,  $\Lambda$ , are given by

$$\begin{aligned} \Lambda_\xi &= D [U, U, U, U+a\sqrt{\xi_x^2+\xi_y^2+\xi_z^2}, U-a\sqrt{\xi_x^2+\xi_y^2+\xi_z^2}] \\ \Lambda_\eta &= D [V, V, V, V+a\sqrt{\eta_x^2+\eta_y^2+\eta_z^2}, V-a\sqrt{\eta_x^2+\eta_y^2+\eta_z^2}] \\ \Lambda_\zeta &= D [W, W, W, W+a\sqrt{\zeta_x^2+\zeta_y^2+\zeta_z^2}, W-a\sqrt{\zeta_x^2+\zeta_y^2+\zeta_z^2}] \end{aligned} \quad (2.4)$$

where D stands for the main diagonal only. It is now possible to introduce 2.3 into 2.2 with the eigenvalues defined in 2.4. By doing so, it is impossible to diagonalize both the convective and diffusive jacobians since they have a totally different set of eigenvectors. By neglecting the diffusive jacobians and assuming the eigenmatrix locally constant, equation 2.2 can be rewritten as

$$T_\xi * [I + \Theta \Delta t (\delta_\xi \Lambda_\xi)] * N * [I + \Theta \Delta t (\delta_\eta \Lambda_\eta)] * P * [I + \Theta \Delta t (\delta_\zeta \Lambda_\zeta)] * T_\zeta^{-1} * \Delta Q = \text{RHS} \quad (2.5)$$

in which the two matrices,  $N = T_\xi^{-1} T_\eta$  and  $P = T_\eta^{-1} T_\zeta$ , have the nice property of being solution independent so that they can be computed only once (ref. 12). Obviously, equation 2.5 is only an approximation of the full form but it requires only scalar tri- or pentadiagonal matrix inversion since the  $\Lambda$  matrices are diagonal; this implies a reduction of nearly 50 percent of the operations required by the standard algorithm. We note that, even though the interior domain is solved implicitly, the boundary conditions are imposed in a fully explicit manner. This was done setting  $\Delta Q = 0$  at the domain boundaries during the implicit sweeps.

### 2.3 - Local Time Stepping

Since the steady state solution is sought, the following local time-stepping formula based on the approximate constant CFL condition is introduced, in which the contribution of the diffusive terms is accounted for as follows:

$$\begin{aligned}
\Delta t_\xi &= |U| + a \sqrt{\xi_x^2 + \xi_y^2 + \xi_z^2} + \mu_{\text{eff}} \text{Re}^{-1} (\xi_x^2 + \xi_y^2 + \xi_z^2) \\
\Delta t_\eta &= |V| + a \sqrt{\eta_x^2 + \eta_y^2 + \eta_z^2} + \mu_{\text{eff}} \text{Re}^{-1} (\eta_x^2 + \eta_y^2 + \eta_z^2) \\
\Delta t_\zeta &= |W| + a \sqrt{\zeta_x^2 + \zeta_y^2 + \zeta_z^2} + \mu_{\text{eff}} \text{Re}^{-1} (\zeta_x^2 + \zeta_y^2 + \zeta_z^2) \\
\Delta t &= \frac{\text{CFL}}{\Delta t_\xi + \Delta t_\eta + \Delta t_\zeta}
\end{aligned}$$

#### 2.4 - Implicit Treatment of Diffusive Terms

For inviscid flows, the only assumption made in deriving the algorithm is that the differentiation of the eigenmatrices is neglected in 2.5. Additionally, when solving the N-S equations, the jacobians of the diffusive terms are normally assumed to be negligible. This does not cause any stability or convergence problems for external flows where the diffusion-dominated region is small and restricted to a limited part of the computational domain. But this simplification may cause troubles for internal flows where the diffusion-dominated region can be large. According to this, for internal flows it is convenient to introduce an approximation of the eigenvalues of the diffusive jacobian and put it into equation 2.5. Two forms of this approximation have been considered.

- Pulliam's Approximation:

Pulliam (ref. 10) proposes an approximate form of the diffusive jacobian eigenvalues that was obtained by intense numerical testing. This form is

$$\begin{aligned}
\Lambda_\xi^v &= (\rho \mu_{\text{eff}} \text{Re}^{-1} (\xi_x^2 + \xi_y^2 + \xi_z^2) J^{-1}) \cdot D[1,1,1,1] \\
\Lambda_\eta^v &= (\rho \mu_{\text{eff}} \text{Re}^{-1} (\eta_x^2 + \eta_y^2 + \eta_z^2) J^{-1}) \cdot D[1,1,1,1] \\
\Lambda_\zeta^v &= (\rho \mu_{\text{eff}} \text{Re}^{-1} (\zeta_x^2 + \zeta_y^2 + \zeta_z^2) J^{-1}) \cdot D[1,1,1,1]
\end{aligned} \tag{2.6}$$

In the present set of calculations it was found convenient not to weight the eigenvalues with the jacobian of the coordinate transformation  $J^{-1}$ . These expressions are included on the implicit side of 2.5. For instance, the  $\xi$  direction implicit operator reads

$$[1 + \Theta \Delta t (\delta_\xi \Lambda_\xi - \delta_\xi^2 \Lambda_\xi^v)]$$

- Present Approximation:

The exact form of the diffusive jacobians can be computed from the related flux vectors. For

the three sweeps, the main diagonal of such a matrix may be conveniently approximated as

$$\begin{aligned}\Lambda_{\xi}^v &= D [0, \alpha_{\xi}, \alpha_{\xi}, \alpha_{\xi}, \gamma \text{ Pr}^{-1} \alpha_{\xi}] \\ \Lambda_{\eta}^v &= D [0, \alpha_{\eta}, \alpha_{\eta}, \alpha_{\eta}, \gamma \text{ Pr}^{-1} \alpha_{\eta}] \\ \Lambda_{\zeta}^v &= D [0, \alpha_{\zeta}, \alpha_{\zeta}, \alpha_{\zeta}, \gamma \text{ Pr}^{-1} \alpha_{\zeta}]\end{aligned}\tag{2.7}$$

in which

$$\begin{aligned}\alpha_{\xi} &= \mu_{\text{eff}} \text{Re}^{-1} \text{J}^{-1} (\xi_x^2 + \xi_y^2 + \xi_z^2) \frac{\partial(\rho^{-1}\text{J})}{\partial \xi} \\ \alpha_{\eta} &= \mu_{\text{eff}} \text{Re}^{-1} \text{J}^{-1} (\eta_x^2 + \eta_y^2 + \eta_z^2) \frac{\partial(\rho^{-1}\text{J})}{\partial \eta} \\ \alpha_{\zeta} &= \mu_{\text{eff}} \text{Re}^{-1} \text{J}^{-1} (\zeta_x^2 + \zeta_y^2 + \zeta_z^2) \frac{\partial(\rho^{-1}\text{J})}{\partial \zeta}\end{aligned}$$

Regarding the extradiagonal terms as negligible, the previous diagonal matrices are a good approximation of the diffusive term jacobians and can be put into the implicit side of 2.5. For instance, the  $\xi$  direction implicit operator reads

$$[ I + \Theta \Delta t (\delta_{\xi} \Lambda_{\xi} - \delta_{\xi} \Lambda_{\xi}^v) ]$$

in which the diffusive terms contribution is approximated as a first-order derivative.

It is possible to prove that the first approximation increases the main diagonal dominance by summing to it an extra term, while in the second approximation an artificial term is subtracted from the off diagonal components while leaving the main diagonal unchanged. A comparison of the two approaches, 2.6 and 2.7, was performed on a simple straight channel geometry at  $\text{Re} \simeq 1000$ ,  $M_{\text{inlet}} = 0.3$  in a laminar flow regime. For this very simple flow configuration there were no differences in convergence rate between the two approaches and it was also possible to drop the diffusive terms on the implicit side without altering convergence. Differences started to appear at  $\text{Re} = 50$  because of the highly diffusive nature of the flow. Figure 1(a) shows the best convergence history of the algorithm without any implicit treatment of the diffusive terms that was obtained at  $\text{CFL} = 5$  (the lower curve refers to the averaged residuals, while the upper one to the maximum). Figures 1(b) and 1(c) refer to equations 2.6 and 2.7. There are no appreciable differences between the two convergence rates obtained at  $\text{CFL} = 10$  since both the curves show nearly the same slope. The same result could be obtained if the Baldwin-Lomax turbulence model were used. At least for this class of flows, the approximate implicit treatment of diffusive terms given by equation 2.7 did not prove to be more efficient than 2.6. Further testing is necessary in order to verify this result at higher Mach numbers when differences in the

convergence between 2.6 and 2.7 may appear since the density derivatives do not tend to vanish for compressible flows as they do for incompressible ones.

## 2.5 - Addition of Explicit and Implicit Damping

When using centered finite differences, it is necessary to introduce an artificial damping scheme in order to prevent odd-even velocity-pressure decoupling that occurs whenever the local Peclet number exceeds two in large gradients regions. Moreover, the three-dimensional approximate factorization method can be proved to be unconditionally unstable since, when performing a linear stability analysis, one of the amplification factors is found to be slightly larger than one. This weak instability can be easily overcome by using an artificial damping scheme. From the two-dimensional version of the approximate factorization, it is also known that fourth-order artificial damping is necessary to damp the numerical modes associated with the highest frequencies. Following the basic guideline given by Jameson et al. (ref. 13) and Pulliam (ref. 14) a blended implicit-explicit second- plus fourth-order nonlinear damping scheme was introduced in the present solver.

### • Explicit Second- and Fourth-Order Damping:

In the original formulation, the artificial damping is simply equally scaled according to the local  $\Delta t$  in the three space directions. This could be done mainly because the damping scheme has been first applied to inviscid flows. For viscous flow calculations, Pulliam (ref. 10) found it convenient to scale the damping terms according to the directional spectral radius  $\sigma$ . The scheme for the  $\xi$  direction sweep yields to

$$D_{\xi}^{(2)} + D_{\xi}^{(4)} = \delta_{\xi} \left( \left( (\sigma J^{-1})_{i+1,j,k} + (\sigma J^{-1})_{i,j,k} \right) \left( \omega_{i,j,k}^{(2)} \delta_{\xi} (Q_{i,j,k}) - \omega_{i,j,k}^{(4)} \delta_{\xi} (Q_{i,j,k}) \right) \right) \quad (2.8)$$

in which the weights  $\omega^{(2)}$  and  $\omega^{(4)}$  are defined as

$$\begin{aligned} \Upsilon_{i,j,k} &= \frac{|p_{i+1,j,k} - 2p_{i,j,k} + p_{i-1,j,k}|}{|p_{i+1,j,k} + 2p_{i,j,k} + p_{i-1,j,k}|} \\ \omega_{i,j,k}^{(2)} &= \Omega^{(2)} \Delta t \max(\Upsilon_{i-1,j,k}, \Upsilon_{i,j,k}, \Upsilon_{i+1,j,k}) \\ \omega_{i,j,k}^{(4)} &= \max(0., \Omega^{(4)} \Delta t - \omega_{i,j,k}^{(2)}) \end{aligned} \quad (2.9)$$

and the unscaled spectral radius is defined as

$$\sigma_{i,j,k} = |U| + a \sqrt{\xi_x^2 + \xi_y^2 + \xi_z^2}$$

Since the present set of calculations has been performed for shock-free flow fields, the shock sensor term defined in 2.9 was switched off, taking always  $\Upsilon_{i,j,k}$ . Nevertheless, this modification does not really affect the damping scheme since the second-order term is active only in presence of shocks. Actually, this scheme gives only fourth-order damping in smooth shock-free flow fields so that in most of the calculations  $\Omega^{(2)}$  was set equal to zero whereas the fourth-order weight,  $\Omega^{(4)}$ , ranges from 1/16 to 1/128. Equation 2.8 is then added to the RHS of 2.5

$$\text{RHS} = \text{RHS} + \Delta t (D_{\xi}^{(2)} + D_{\xi}^{(4)} + D_{\eta}^{(2)} + D_{\eta}^{(4)} + D_{\zeta}^{(2)} + D_{\zeta}^{(4)})$$

• Implicit Second- or Fourth-Order Damping:

To enhance the algorithm stability and convergence rate, it is helpful to include the artificial damping terms on the implicit side. For both the second- and fourth-order damping, the implicit treatment augments the diagonal dominance of the scalar system with a beneficial effect on the convergence rate. As was pointed out by Pulliam (ref. 10), there is a stability limit for the weights that can be used for the artificial damping terms. This limit is actually connected to the magnitude of the amplification factor of the scheme modified with the artificial terms. To obtain the best convergence rates, the implicit damping had to be the exact jacobian of the explicit counterpart added to the right-hand side. If the second-order damping is treated implicitly, equation 2.5 must be modified to include the added implicit terms. For instance, the  $\xi$  sweep implicit side will be

$$\left\{ I + \Theta \Delta t \left( \delta_{\xi} \Lambda_{\xi} - \delta_{\xi} \left( ((\sigma J^{-1})_{i+1,j,k} + (\sigma J^{-1})_{i,j,k}) (\omega_{i,j,k}^{(2)} \delta_{\xi}^2 J_{i,j,k}) \right) \right) \right\} \quad (2.10)$$

This form maintains the tridiagonal nature of the jacobian matrix.

When the fourth-order damping is treated implicitly, the differentiation of the jacobian matrix gives a scalar pentadiagonal system that, for the  $\xi$  sweep, can be written as

$$\left\{ I + \Theta \Delta t \left( \delta_{\xi} \Lambda_{\xi} - \delta_{\xi} \left( ((\sigma J^{-1})_{i+1,j,k} + (\sigma J^{-1})_{i,j,k}) (\omega_{i,j,k}^{(4)} \delta_{\xi}^3 J_{i,j,k}) \right) \right) \right\} \quad (2.11)$$

A brief set of tests on a straight channel geometry proved that the fourth-order implicit damping (eq. 2.11) could bring a large gain in convergence rate with respect to the second-order (eq. 2.10). For a straight three-dimensional channel with approximately  $10^4$  points with an inlet-section-width to channel-length ratio of 15, typical of internal flow geometries, the tridiagonal solver associated with equation 2.10 could be run at CFL=2, which gives the convergence history shown in figure 2(a), while the pentadiagonal solver associated with equation 2.11 was shown to be much more robust and gave the much higher convergence rate shown in figure 2(b) with CFL=10. Despite a 25 percent increase in computational time to invert the pentadiagonal matrix with respect to the three-diagonal one, the implicit fourth-order option proved to be much faster and more robust, and was retained in all the calculations.

• Wall Treatment of Artificial Damping:

It is well known that any kind of artificial damping term introduces an error that has to be minimized in order not to affect the solution heavily. Among the various approaches that can be found in the literature, the nonlinear damping formulation proposed by Jameson et al. (ref. 13) ensures that the second-order terms are introduced only at shocks while keeping the fourth-order in the smooth region of the computational domain. However, it is possible to prove that, if the presence of the boundaries is not properly accounted for when introducing the artificial terms, nonzero momentum and mass fluxes can be produced at the boundaries. This fact can be easily seen by considering figures 3(a) and (b). Figure 3(a) shows the fourth-order damping weights applied at every single point  $i$  for the  $\xi$  direction. The fourth-order difference stencil used here is

$$\delta_{\xi}^4(Q_{i,j,k}) = Q_{i-2,j,k} - 4 Q_{i-1,j,k} + 6 Q_{i,j,k} - 4 Q_{i+1,j,k} + Q_{i+2,j,k}$$

The fourth-order damping is normally switched off at  $i=1$  and  $i=2$  so that no special treatment at the wall is required. Figure 3(a) shows that in doing so the sum of the fourth-order damping weights for every location  $i$  is zero only in the internal flow field for  $i \geq 5$ . This ensures that no net fluxes are added in the internal domain only, while the sum of the artificial damping weights yields to nonzero values for  $1 \leq i \leq 4$ . These weights actually correspond to a nonzero third-order derivative centered at  $i=(2+1/2)$ . The same procedure may be followed for the second-order damping that is switched off at  $i=1$  (fig. 3(b)). The sum of the weights for every location  $i$  is zero only for  $i \geq 3$ . This gives a first-order derivative centered at  $i=1/2$  that corresponds to a first-order flux at the wall. These flux errors can be easily controlled in two dimensions by a grid refinement in the wall proximity where high gradients are expected. In three-dimensional internal flows we are forced to use coarser grids, and the wall boundary condition is applied on very large surfaces with the possible result of large mass errors. To control the mentioned flux errors, a third-order derivative, with the differencing stencil given by

$$\delta_{\xi}^3(Q_{i,j,k}) = -Q_{i-1,j,k} + 3 Q_{i,j,k} - 3 Q_{i+1,j,k} + Q_{i+2,j,k}$$

was added at  $i=2$  to balance the fourth-order damping weight. The procedure was followed to balance the second-order damping at the wall where a first-order derivative, with the differencing stencil given by

$$\delta_{\xi}(Q_{i,j,k}) = -Q_{i-1,j,k} + Q_{i,j,k}$$

was added at  $i=2$ .

## Chapter 3

# TURBULENCE MODELS

### 3.1 - Baldwin-Lomax for Multiple Boundaries

The standard version of the Baldwin-Lomax (ref. 4) zero-equation turbulence model was implemented here. This two-layer model divides the flow field into an inner layer close to the wall (in which viscous effects are dominant) and an outer layer. The two layers are governed by the following set of equations and constants.

- Inner Layer:

$$\mu_{t,inner} = Re \rho l^2 |\omega|$$

$$l = K y D$$

$$D = (1 - \exp(-y^+/A^+))$$

$$y^+ = y \sqrt{Re \omega_{max}}$$

in which  $\Omega$  is the vorticity,  $D$  is the Van Driest damping function,  $y$  is the wall distance and  $K=0.41$  is the Von Karman constant.

- Outer Layer:

The outer viscosity is applied from the point at which  $\mu_{t,inner} = \mu_{t,outer}$ :

$$\mu_{t,outer} = Re \rho K_c C_{cp} F_{wake} F_{kleb}(y)$$

in which  $K_c=0.0168$  is the Clauser constant and  $C_{cp}=1.6$  is an empirical constant; and

$$F_{wake} = \min(y_{max} F_{max} ; 0.25 y_{max} U_{dif}^2 F_{max})$$

in which  $F_{max}$ ,  $U_{dif}$  and  $F_{kleb}$  are given by

$$F(y) = y |\omega| D$$

$$U_{dif} = (\sqrt{U^2 + V^2 + W^2})_{max} - (\sqrt{U^2 + V^2 + W^2})_{min}$$

$$F_{kleb} = \frac{1}{1 + 5.5 (C_{kleb} y / y_{max})}$$

where  $C_{kleb}=0.3$ , and  $y_{max}$  is the wall distance at which  $F(y)$  is maximum.



This algebraic turbulence model was originally developed for a single boundary layer, but in three-dimensional internal flows the presence of multiple boundaries causes the interaction of more than one boundary layer. While the inner, or viscous, layer is driven by what happens on the closest wall only, for the outer layer an averaging procedure is necessary to account for the various wall effects. In the present set of calculations, three approaches have been examined to account for the presence of more than one boundary layer.

- Wall Treatment 1:

Only the geometrically closest wall is considered for computing the outer viscosity without any averaging.

- Wall Treatment 2:

The inner layers are driven by the closest wall only, while the viscosity in the outer layer is computed with a simple weighted average according to the inverse of each wall distance as follows

$$\mu_{t,outer} = \frac{1}{\sum_w \frac{1}{W_w}} \sum_w \left( \frac{\mu_{t,outer}^w}{W_w} \right)$$

where  $W_w$  is the wall distance,  $w$  is the wall number, and  $N$  is number of walls present in a cross section.

- Wall Treatment 3:

If only one boundary layer is present, the Van Driest damping succeeds in modeling the wall effect. Starting from this standpoint, the inner layer viscosities are computed by using only the closest wall contribution, while the viscosity in the outer layer is computed as a simple weighted average according to the inverse of the value of the Van Driest damping expression for each wall.

### 3.2 - $q-\omega$ Two-Equation Model

In a previous investigation, Michelassi (ref. 7) found that the low Reynolds number forms of the two-equation models, such as  $k-\epsilon$ , could give an accurate prediction of two-dimensional incompressible separated flows. Unfortunately, these forms were found to be numerically stiff, mainly because of the correction terms introduced to model the low Reynolds effects that necessitate a strong mesh refinement in the sublayer. Furthermore, an initial profile for the turbulent quantities must be specified consistently to start the calculations. A first attempt to implement the Chien and the Rodi two-layer low Reynolds number forms of the  $k-\epsilon$  model did not bring any converged result mainly because of difficulties in specifying both the mesh refinement and initial profiles for complex three-dimensional flows. Coakley (ref. 15), reassembling the Jones and Launder low Reynolds number form of the  $k-\epsilon$  model, proposed the  $q-\omega$  two-equation model, in which the effect of molecular viscosity is directly modeled. This formulation ensured a better numerical behavior as compared with other low Reynolds number formulations. This model, rewritten in our notation, is

$$\frac{\partial \bar{Q}}{\partial t} + \frac{\partial \bar{E}}{\partial \xi} + \frac{\partial \bar{F}}{\partial \eta} + \frac{\partial \bar{G}}{\partial \zeta} = \frac{\partial \bar{E}_v}{\partial \xi} + \frac{\partial \bar{F}_v}{\partial \eta} + \frac{\partial \bar{G}_v}{\partial \zeta} + \bar{H} \quad (3.1)$$

where the flux vectors are defined as

$$\begin{aligned} \bar{Q} &= J^{-1} \begin{bmatrix} \rho q \\ \rho \omega \end{bmatrix} \\ \bar{E} &= J^{-1} \begin{bmatrix} \rho U q \\ \rho U \omega \end{bmatrix} \quad \bar{F} = J^{-1} \begin{bmatrix} \rho V q \\ \rho V \omega \end{bmatrix} \quad \bar{G} = J^{-1} \begin{bmatrix} \rho W q \\ \rho W \omega \end{bmatrix} \\ \bar{E}_v &= \frac{J^{-1}}{Re} \begin{bmatrix} (\mu + \frac{\mu_1}{\sigma})(\xi_x q_x + \xi_y q_y + \xi_z q_z) \\ (\mu + \frac{\mu_1}{\sigma})(\xi_x \omega_x + \xi_y \omega_y + \xi_z \omega_z) \end{bmatrix} \\ \bar{F}_v &= \frac{J^{-1}}{Re} \begin{bmatrix} (\mu + \frac{\mu_1}{\sigma})(\eta_x q_x + \eta_y q_y + \eta_z q_z) \\ (\mu + \frac{\mu_1}{\sigma})(\eta_x \omega_x + \eta_y \omega_y + \eta_z \omega_z) \end{bmatrix} \\ \bar{G}_v &= \frac{J^{-1}}{Re} \begin{bmatrix} (\mu + \frac{\mu_1}{\sigma})(\zeta_x q_x + \zeta_y q_y + \zeta_z q_z) \\ (\mu + \frac{\mu_1}{\sigma})(\zeta_x \omega_x + \zeta_y \omega_y + \zeta_z \omega_z) \end{bmatrix} \\ \bar{H} &= J^{-1} \begin{bmatrix} \frac{1}{2}(C_\mu \frac{D}{\omega^2} P - 1 - \frac{2}{3} \frac{P}{\omega} \frac{d}{\omega}) \rho \omega q \\ (C_1(C_\mu \frac{P}{\omega^2} - \frac{2}{3} \frac{P}{\omega} \frac{d}{\omega}) - C_2) \rho \omega^2 \end{bmatrix} \end{aligned}$$

in which

$$D = 1 - e^{-\alpha R}$$

$$R = Re \rho q y$$

$$P_d = \frac{\partial U_i}{\partial x_i}$$

$$S = \left( \frac{\partial U_i}{\partial x_j} + \frac{\partial U_j}{\partial x_i} - \frac{2}{3} \delta_{ij} P_d \right) \frac{\partial U_i}{\partial x_j}$$

$$P = \mu_t S - \frac{2}{3} k P_d$$

$$C_1 = 0.405 D + 0.045$$

$$C_\mu = 0.09 ; C_2 = 0.92 ; \alpha = 0.0065 ; \sigma_q = 1.0 ; \sigma_\epsilon = 1.3$$

The turbulent viscosity is computed as

$$\mu_t = Re C_\mu D \frac{\rho k}{\omega}$$

The two transported quantities,  $q$  and  $\omega$ , are related to the more familiar  $k$  and  $\epsilon$  via the following relations:

$$q = k^{1/2} ; \omega = \epsilon / k \quad (3.2)$$

It is important to observe that  $\epsilon$ , appearing in equation 3.2, is the isotropic part of the dissipation rate. This quantity does not account for any nonisotropic effect (for example, the presence of a wall) and tends to zero on solid boundaries. (Conversely, the total dissipation rate tends to a finite value related to the wall shear stress.) This choice allows use of  $\omega$  as an unknown since, by assuming that both  $k$  and  $\epsilon$  are going to zero at the wall with the same slope,  $\omega$  tends to a finite value.

### 3.2.1 - $q$ - $\omega$ Solution

The two transport equations for  $q$  and  $\omega$  are implicitly solved with the same algorithm given in equation 2.2. The two equations are solved in a sequential manner and decoupled from the flow variables mainly because the coupling is provided only by the diffusive terms coefficients and the sink and source terms. Due to this choice, the scalar tridiagonal algorithm was implemented for the turbulence model solution. The only difference with respect to the solution of the N-S equations is the presence of the sink-source vector  $\bar{H}$ . This term can be included in the three sweeps:

$$\begin{aligned}
& [I + \Theta \Delta t (-H_j c_\xi + \delta_\xi A - \delta_\xi^2 A_v)] * \\
& [I + \Theta \Delta t (-H_j c_\eta + \delta_\eta B - \delta_\eta^2 B_v)] * \\
& [I + \Theta \Delta t (-H_j c_\zeta + \delta_\zeta C - \delta_\zeta^2 C_v)] * \Delta Q = \text{RHS}
\end{aligned} \tag{3.3}$$

where the same definitions given for equation 2.2 hold with only the addition of the jacobian of the sink and source terms,  $H_j$ , that is weighted in three sweeps according to  $c_\xi$ ,  $c_\eta$ ,  $c_\zeta$  ( $c_\xi + c_\eta + c_\zeta = 1$ ). This jacobian is computed by neglecting the contribution of the damping function  $D$ , and for the two  $q$  and  $\omega$  equations reads

$$\begin{aligned}
H_j^q &= \frac{\partial H^q}{\partial(\rho J^{-1} q)} = \frac{1}{2} \frac{C_\mu DS}{\omega} - \frac{1}{3} P_d - \frac{\omega}{2} \\
H_j^\omega &= \frac{\partial H^\omega}{\partial(\rho J^{-1} \omega)} = -\frac{2}{3} C_1 D P_d - C_2 2\omega
\end{aligned}$$

In place of their exact form, Coakley proposes an approximation of the jacobians based on the turbulent viscosities that should ensure the dominance of the main diagonal. Figure 4 shows the comparison of the convergence rates of every single variable obtained without any sink or source terms jacobian, with the exact jacobian, and with Coakley's approximation in a typical internal flow geometry. Surprisingly, there is no big gain in introducing the jacobian in the implicit side of the operator. The choice of the sweeps in which the two jacobians  $H_j^q$  and  $H_j^\omega$  are introduced is not important. The error introduced in the approximate factorization of the implicit side of 3.3 increases roughly by a factor proportional to  $H_j$  when introducing the jacobian in the three sweeps, thereby choosing  $c_\xi = c_\eta = c_\zeta = 1/3$ . This has only a weak influence on the convergence rate. Nevertheless, in the present calculations the best convergence rates have been typically obtained by using  $c_\xi = 0$ ,  $c_\eta = 0.5$ , and  $c_\zeta = 0.5$ , where  $\xi$  is the main flow direction and  $\eta, \zeta$  are the fine grid directions.

While physical evidence shows that the turbulent kinetic energy  $k$  is zero at solid walls, the boundary condition for  $\epsilon$ , and consequently  $\omega$ , is less evident. For the  $q$ - $\omega$  model, Coakley (ref. 15) found it convenient to impose a zero-normal derivative at the wall; this condition was retained in the present calculations.

## Chapter 4

# RESULTS

### 4.1 - Incompressible S-duct

A first validation of the code was performed by computing the flow in an S-duct with a constant area cross section. The measurements (ref. 16) were taken for an incompressible fluid (water). The S-duct was given by two 22.5 degree bends with a 4-cm hydraulic diameter and 28-cm mean radius of curvature. This geometry was regarded as an interesting test since flow passages with similar shapes are often used to redirect the flow for air intakes in aeronautical engines. The efficiency of such ducts may be heavily affected by the presence of secondary flows so that the ability of a code to detect secondary velocities is essential for a proper depiction of the flow pattern.

A sketch of the flow domain is shown in figure 5. Since the geometry and the flow were symmetric with respect to the x-r plane, it was possible to study only one-half of the duct imposing a symmetry boundary condition on the same plane. For the laminar flow regime, the Reynolds number,  $Re$ , based on the inlet bulk velocity,  $U_b$ , and hydraulic radius was 790. The grids employed for this calculation are shown in figures 6(a) and (b). The coarser grid (fig. 6(a)) has  $70 \times 29 \times 15$  points with a ratio between two consecutive grid cells in the cross-flow directions of 1.1 while the refined one (figure 6(b)) has  $80 \times 59 \times 30$  points with the same stretching ratio in the cross-flow plane. The fluid adopted in the experiments was water so that, in order to have negligible compressibility effects, the isentropic Mach number was set equal to 0.1 (that gives the inlet total pressure, outlet static pressure ratio) to ensure minor density changes.

The flow pattern and the growth of the secondary motions are mainly pressure-driven because of the very smooth-bending walls that cause no flow separation. Still, this kind of flow necessitates a very accurate prediction of the boundary layer, even in the laminar regime, otherwise the secondary flows may be incorrectly predicted or completely lost. Figure 7(a) shows the measured (circles) and computed velocity profiles with the two grids mentioned above for the five sections, indicated in figure 5, on the symmetry plane reported in the experiments. The slight discrepancies in the computed velocities with the two grids at section 1, where the double-S starts, may be attributed to the thinner boundary layer predicted with the refined grid that produced a flatter velocity profile. Nevertheless, the agreement with experiments is fairly good. The agreement does not deteriorate for sections 2, 3, and 4 in either the coarse or refined grids. Section 5 clearly shows that while the secondary motions could not be predicted by the coarse grid, they are fairly well reproduced by the refined one. This behavior is thought to be independent of the grid points in the main flow direction (as will be demonstrated in a further test) in which only 10 points are added in the refined grid, and is closely related to the poor resolution of the boundary layer provided by the coarse grid in which the cross-flow momentum diffusion is clearly overestimated.

Figure 7(b) shows the velocity profiles for the midspan section ( $r=1/2$ ) at the same five sections. Basically the same comments made for the symmetry plane could be repeated here for the first three sections, while on sections 4 and 5, agreement deteriorates in the proximity of the symmetry plane. This may be attributed not only to the poor grid quality close to the symmetry

plane, but also to the fact that in the calculations a zero gradient condition was imposed in the direction normal to that plane, while experiments show that for section 4 the velocity gradient is far from being zero on the same plane. The typical computed secondary motion pattern at the exit of the second bend is shown in figure 7(c). The complex flow pattern exhibits two counterrotating vortices in the proximity of the two curved walls.

Nearly 1500 iterations were necessary to reach an averaged residual of the order of  $10^{-5}$  on the refined grid, while typically less than half that number of iterations were necessary to obtain the same residual with the coarser grid. These calculations were performed with an early version of the code where only the second-order implicit damping was implemented, so that the slow convergence rate may be attributed to both the small Mach number and to the small CFL number that could not exceed 2 without encountering stability problems.

The turbulent flow regime was run at the experimental condition of  $Re=40.000$ . For this calculation, it was necessary to provide a more stretched grid at the wall, so that the  $80 \times 59 \times 30$  grid was reassembled with a point expansion ratio in the cross-flow directions equal to 1.3. This provided the necessary point clustering at the boundaries to describe the thin boundary layer and allowed placing the first point at the wall at  $y^+ \approx 2$ . For this test case, the Baldwin-Lomax model was implemented with wall treatment number 1. (See the section on Baldwin-Lomax for multiple boundaries.)

Figure 8(a) shows the set of measured and computed velocity profiles on the symmetry plane for the same five cross sections given in figure 5. For this flow configuration, the agreement is reasonably good, especially at cross sections 4 and 5. In these sections the pressure gradients induce a strong secondary motion that seems to be correctly predicted by the present solver insofar as the agreement with measurements does not deteriorate as the second bend exit is approached and the secondary velocities reach their maximum. The momentum transfer to the external part of the second bend, particularly evident in sections 4 and 5, is well reproduced since the computed velocity profile asymmetry seems to be in close agreement with experiments.

Figure 8(b) shows the computed and measured velocities on the midspan plane along the duct. The agreement is again good for the five sections and better than that found for the laminar flow regime mainly because the measured velocity profiles exhibit a zero-gradient on the symmetry plane that is correctly modeled by the symmetry condition imposed on the x-r plane. Still, at sections 3 and 4, the kink in the velocity profile close to the wall is not correctly predicted.

The static pressure coefficient in the main flow direction, defined as

$$C_p = \frac{P - P_{inlet}}{\frac{1}{2} \rho U_b^2}$$

is shown figure 8(c) at three different locations ( $z=0, r=0$ ), ( $z=0, r=1$ ), and ( $r=1/2, z=1/2$ ). Here the agreement is generally good. The pressure trend is correctly predicted together with the head loss.

Figure 8(d) shows the convergence history obtained with  $CFL=2$ . For this calculation, the

same early version of the code mentioned above was used. The solid upper line refers to the maximum residual while the dashed line refers to the averaged residual; the spikes present in the first curve correspond to the updating of the turbulent viscosity performed every five iterations. It is remarkable that the pressure distribution did not change after the first 500 iterations, while to get the correct velocity profiles, it was found necessary to reach a residual of the order of  $10^{-5}$  to  $10^{-6}$ .

#### 4.2 - Stanitz Elbow

The flow in the accelerating rectangular elbow with 90 degree turning and the variable cross section described by Stanitz (ref. 17) has been computed with an inviscid version of the code and with both the Baldwin-Lomax and  $q-\omega$  turbulence models. This test case was selected because it provides a good set of measurements, including wall pressure distribution and visualization of secondary flows at the elbow exit section. The shape of the elbow was analytically computed by Stanitz (ref. 17) to give no separation with a strong area reduction and a specified pressure distribution on the side wall under incompressible flow conditions. A sketch of the experimental setup is shown in figure 9. Both the flow and the elbow geometry are symmetric with respect to the x-y midspan plane, thereby allowing a zero normal gradient condition. Among the various flow conditions investigated in reference 17, the one with  $M_{exit}=0.4$  and with no spoiler at the duct inlet with a thin initial boundary layer was selected.

##### 4.2.1 - Inviscid Calculations

The first set of tests was performed with an inviscid version of the code. The convergence characteristics of the scalar form of the approximate factorization could be tested for inviscid calculations where the necessity of accounting for the diffusive terms on the implicit side of equation 2.5 drops. Only the pressure distribution on the walls of the elbow was compared with measurements in this set of calculations; no attempt was made to specify an experimental inlet profile of total pressure that was kept flat. The inlet boundary condition was specified by extrapolating the Riemann invariant from the first section inside the duct (ref. 18). Two grids were used: a  $25 \times 15 \times 11$  and a  $50 \times 15 \times 11$  with constant grid spacing in the cross-flow directions. The grid point locations in the streamwise direction were made to coincide with the points supplied by Stanitz (ref. 17) for the description of the elbow geometry, with the addition of three sections at the outlet to allow using a zero gradient condition.

Figures 10(a) and (b) show the qualitative static pressure and Mach number isolines on the symmetry plane of the elbow. The small wiggles visible at the domain exit are due to the very small fourth-order damping weight that was set equal to  $\Omega^{(4)}=1/256$ , together with  $\Omega^{(2)}=0$ . The small value of the fourth-order damping weight is allowed by the very coarse grid in the cross-flow direction that automatically introduced a numerical diffusion. Despite the very coarse grids implemented here, the static pressure distribution  $p_s$ , defined as

$$p_s = \frac{P - P_{exit}}{P_{total} - P_{exit}}$$

and shown in figures 11(a) and (b), reveals fairly good agreement with experiments. While the pressure drop position is located correctly for the two grids on both the side and symmetry walls, the kink in the static pressure distribution on the suction surface at the side wall could not be reproduced since it was caused by the presence of secondary flows. The pressure distribution appears to be independent of secondary flows induced by viscous effects until the first part of the bend is reached. The local pressure rise located at  $S=2$ , where  $S$  is the streamwise coordinate along the centerline, is introduced by the growth of secondary velocities and is totally lost by the inviscid solver. The solution proved also to be fairly grid-independent, at least to the grid refinement in the main flow direction. No additional tests were performed to verify the influence of the point distribution in the cross-stream direction.

The implicit treatment of second- and fourth-order artificial damping was compared by using the  $50 \times 15 \times 11$  grid. Figure 12 shows the comparison between the two implicit damping schemes. The solid line refers to the second-order implicit damping with  $\Omega^{(2)}=1/4$ , while the dashed line refers to the fourth-order implicit option with  $\Omega^{(4)}=1/256$ . The gain in convergence rate is remarkable; in fact, the fourth-order solver could be run at  $CFL=10$  while the second-order one could not be run at  $CFL \geq 5$ . Any further increase of the artificial damping weights gave slower convergence histories. Unfortunately, the same convergence rate is not obtainable for viscous calculations because of the strong point clustering and viscous effects that are not exactly accounted for on the implicit side of the operator.

#### 4.2.2 - Viscous Calculations

The viscous calculations in the turbulent flow regime were performed on the five grids summarized in table I. The use of various point clusterings allowed a comprehensive investigation into the mesh dependence of the calculations. With this set of grids, it was possible to verify the influence of the grid point numbers in the main flow direction (with 51 or 99 points) and the cross-flow direction (with  $31 \times 21$  and  $41 \times 31$  points) with expansion ratios of 1.2 and 1.3. The refined grid (number 5) shown in figure 13 adopts the same point distributions in the main flow direction that were used for the refined grid in the inviscid calculations, and allows placing the first grid point at the wall at  $y^+ \approx 1$ . The Reynolds number, based on the total conditions at the inlet section, is approximately  $2.5 \cdot 10^6$ .

These calculations were mainly aimed at the proper prediction of the wall pressure distribution that is heavily affected by the growth of secondary velocities. The choice of the experimental spoilerless configuration allowed comparing the turbulence models for a very thin boundary layer that required a heavy point stretching at the wall. Regarding the inlet boundary condition, in the Baldwin-Lomax model the inlet turbulent viscosity was extrapolated from inside the domain, and in the  $q-\omega$  model a flat turbulent kinetic energy profile with various turbulence levels was specified at the inlet section, while  $\omega$  was extrapolated from inside the domain.

The first set of tests concerned the Baldwin-Lomax model with the different wall treatments mentioned in section 3.1. With the experimental total pressure profile specified at the inlet section, the computed static pressure profiles are compared with the measurements in figure 14. The plots refer to the static pressure distribution in the section corners on the side wall and the symmetry plane. It is evident that the way the outer viscosity is computed may play a significant role in the correct prediction of the pressure distribution. Wall treatment number 1, in which only



the closest wall is considered, and number 2, in which the outer turbulent viscosity is weighted according to the inverse of the wall distance, do not show large changes even if the two approaches are considerably different. For both techniques, the agreement with experimental results is fairly good on the pressure side of both the side wall and the symmetry plane. The suction side on both planes shows that the static pressure is overestimated. This is probably due to the presence of computed secondary flows that are much stronger than the experimental ones. The computed pressure drop induced by the presence of the bend and the strong flow acceleration is smoother than the measured one. This phenomenon is caused by high turbulent viscosities that induce a heavy momentum diffusion in the cross-flow direction, followed by a static pressure redistribution and growth of the boundary layer thickness. The agreement with measurements improves with multiple wall treatment number 3. No great changes between the multiple wall treatments are found for the pressure side of both the side wall and the symmetry plane where it was always possible to have accurate results. Still, the pressure minimum located at  $S=2$ , where velocities on the cross section start to develop, is better reproduced by wall treatment number 3. This test suggests that the averaging technique based on the Van Driest damping expression for the mixing length can give reasonable predictions. All the computations with the Baldwin-Lomax model were performed with multiple wall treatment number 3.

The results of the mesh dependence tests for the Baldwin-Lomax model are summarized in figure 15 where the computed static pressure distribution in the four corners of the cross sections using different grids are compared with measurements. The pressure distribution profiles show that there are practically no differences between the predictions obtained with grids number 1 and 3. This proves that an increment of the grid point numbers in the main flow direction does not produce any gain in terms of accuracy. This is strictly connected to the boundary layer resolution that is not improved by using grid number 3. The secondary flow growth is influenced by the low momentum regions located close to the wall, the correct simulation of which is not ensured by the two grids. Conversely, the implementation of grid number 2 clearly improves the accuracy of the results. The static pressure profile on the suction side of the side wall is in better agreement with experiments than the pressure distributions given by grids number 1 and 3. It is worthwhile observing that the use of a more refined grid in the cross-flow direction shows that the computed pressure minimum on the suction side is correctly located, even if its value is still overestimated, while this local minimum, located approximately at  $S=2$ , is completely lost with the other two grids. Nevertheless, the static pressure distribution on the symmetry plane appears to be weakly affected by grid refinement. No further investigation was performed by varying the cross-flow points expansion ratio.

The flow simulation with the  $q-\omega$  model required more tests since it has been necessary to investigate the dependence on both the mesh refinement and on the inlet turbulence level. The use of grids with an expansion ratio equal to 1.2 did not ensure significant improvements in results since not enough points were located close to the wall. In order to have a reasonable definition of the turbulent kinetic energy peak at the wall, the grid expansion ratio was fixed at 1.3. The results of the first set of tests are summarized in figure 16 in which, by adopting the coarse grid number 4, the inlet turbulence level was changed to verify its influence on the static pressure distribution. When decreasing the inlet turbulence level from 5.0 to 0.1 percent, the computed profiles progressively approach the measurements. Still, the predictions are far from the experiments for the suction side of both the symmetry plane and the side wall. This indicates the presence of a large momentum diffusion that is possibly caused by insufficient mesh refinement or

too high a turbulence level, or both. Figure 17 shows the results obtained with grid number 5 and lower turbulence levels. Figures 16 and 17 show that the refined grid with the same turbulence level brings some improvement in the agreement with the experiments, proving that the coarser grid was largely inadequate for this flow configuration (see, for instance, the 0.1 percent level). The growth of the secondary flows is evident in figure 17 where the static pressure distribution computed with the inviscid approach is compared with the results of the two-equation model obtained with different turbulence levels.

A direct comparison of the turbulent calculations with the inviscid computation, in which the same pressure distribution is found on both the side wall and the symmetry plane because of the absence of secondary motions, shows large differences on the suction side only. These differences start from  $S=2$  where experiments deviate from the inviscid solution. The one percent turbulence level, not reported in figure 17, appeared to bring too high a momentum diffusion. Consequently, this level was progressively decreased from 0.5 to 0.1 percent. The static pressure distribution on the pressure wall is mainly driven by convective phenomena, while the distribution on the suction wall is largely influenced by diffusion processes; this is why the pressure side distribution is always well reproduced and is nearly independent of the inlet turbulence level. The final result obtained with grid number 5 and a 0.1 percent turbulence level shows a fairly good agreement with experiments on both the suction and pressure sides, and seems to reproduce quite correctly the location and influence of secondary flows.

The predicted pressure distributions obtained by the Baldwin-Lomax model with wall treatment number 3 and the  $q-\omega$  model were very similar, but the two-equation model proved to be marginally more accurate, especially because of the static pressure distribution on the suction side. Figure 18 shows that the two models predict approximately the same static pressure pattern on the symmetry plane with nearly the same pressure drop due to the acceleration on the flow. Still, from figure 19, where the Mach number isolines are shown on the same symmetry plane, it is possible to observe that the zero equation model predicts a slightly thicker boundary layer than the one predicted with the  $q-\omega$ . These differences start immediately after the inlet section and become more evident as the exit section is approached. This indicates a different turbulent viscosity distribution in the wall region. The Baldwin-Lomax model was in fact found to predict a sharper growth of the turbulent viscosity in the wall region. Still, the two models gave comparable values of the turbulent viscosity in the flow core. The differences in the boundary layer thickness are evident in figure 20 where the velocities in the exit section of the channel are plotted. While both turbulence models show the same flow pattern, the two-equation model predicts the center of the secondary recirculation closer to the wall than that predicted by the zero-equation model, in which the location of the center appeared to be in better agreement with experiments. This confirms a weaker cross-flow momentum diffusion (given by the two-equation model) as compared with the zero-equation. This is caused by the aforementioned differences in the turbulent viscosities. It is remarkable that both formulations predict a small secondary vortex in the wall corner of the suction and pressure walls.

An interesting qualitative comparison of the predicted and measured secondary flows is given by figure 21. Figure 21(a) shows the experimental flow visualization by injecting a smoke filament inside the boundary layer close to the side wall at the inlet section of a reduced model of the channel. The low-momentum particles located well within the boundary layer are bent toward the suction wall by the pressure gradients, while the high-momentum particles exhibit a weaker

turning. Figure 21(b) shows the secondary flow predicted by the zero equation model, while figure 21(c) refers to the results obtained with the  $q-\omega$  model. From this comparison, it is evident that the zero-equation model predicts a smoother turning of the velocities. This is in slightly better agreement with the experimental picture than the  $q-\omega$  model.

A typical total pressure loss distribution on the channel exit section is given in figure 22. The results computed with the Baldwin-Lomax model using grids number 1 and 2 show the much thicker boundary layer obtained with the coarser grid. The refined grid ensures a correct description of secondary flows together with the location and magnitude of the total pressure losses.

With the present research version of the code, 6000 sec were necessary to perform 2500 iterations with the  $q-\omega$  turbulence model with a 63.550 point grid on a CRAY-YMP supercomputer. This ensured an overall residual of the order of  $10^{-6}$ , while a reduction of approximately 30 percent in CPU time could be obtained by using the zero-equation model. As mentioned by Coakley (ref. 15), the  $q-\omega$  model was found to be remarkably insensitive to the initial field that is specified to start the calculations for  $q$  and  $\omega$ . In the present tests it has always been possible to start the model with a flat distribution of the turbulence quantities. For the viscous calculations, it was a good practice to keep  $CFL \leq 10$  together with  $1/32$  as a weight for the fourth-order artificial damping. The total absence of shocks allowed for eliminating the second-order artificial damping in all the calculations. Moreover, the aforementioned wall treatment of the fourth-order damping ensured inlet-outlet mass errors of the order of 0.5 percent.

## Concluding Remarks

The scalar form of the approximate factorization coupled with a turbulence model proved to be suited for the solution of turbulent internal flows where diffusive terms play a dominant role. The introduction of an approximate treatment of the diffusive terms proved to increase convergence of the algorithm for internal flow configurations. Nevertheless, the implicit treatment of these terms must be tested for a wider range of geometries and Reynolds numbers. The influence of Mach number on convergence rate needs to be investigated, especially for the proposed approximate implicit treatment of diffusive terms based on a space derivative of the fluid density. New tests are currently being performed.

For the Stanitz elbow geometry, the Baldwin-Lomax turbulence model proved to give results in acceptable agreement with the experiments, provided that the presence of multiple boundaries is properly accounted for. The low Reynolds number  $q-\omega$  two-equation model version investigated here proved to be suited for three-dimensional computations and gave a satisfactory description of the flow field with a manageable number of grid points and only a small increase in computational time with respect to the algebraic model.

## References

1. Pulliam, T.H.; and Steger, J.L.: Implicit Finite Difference Simulations of Three-Dimensional Compressible Flow. *AIAA J.*, vol. 18, no. 2, Feb. 1980, pp. 159-167.
2. Kreamer, J.C., et al.: Experimental/Computational Study of Viscous Flow in a Contracting Rectangular Elbow. *AIAA J.*, vol. 26, no. 12, Dec. 1988, pp. 1434-1441.
3. Yokota, J.W.: A Diagonally Inverted LU Implicit Multigrid Scheme for the 3-D Navier-Stokes Equations and a Two Equation Model of Turbulence. NASA CR-182209, 1988 (AIAA Paper 88-0467).
4. Baldwin, B.S.; and Lomax, H.: Thin Layer Approximation and Algebraic Model for Separated Turbulent Flows. *AIAA Paper* 78-257, Jan. 1978.
5. Chima, R.V.; and Yokota, J.W.: Numerical Analysis of Three-Dimensional Viscous Internal Flows. NASA TM-100878, 1988.
6. Towne, C.E.: Computation of Viscous Flow in Curved Ducts and Comparison with Experimental Data. NASA TM-83548, 1984 (AIAA Paper 84-0531).
7. Michelassi, V.: Testing of Turbulence Models with an Artificial Compressibility Solution Method. Report SFB (Sonderforschungsbereich, University of Karlsruhe) 210 T49, University of Karlsruhe, Karlsruhe, West Germany, Jan. 1989.
8. Martelli, F.; and Michelassi, V.: An Implicit Factored Solver for Inner Turbulent Flows. *AIAA Paper* 88-3099, July 1988.
9. Rodi, W.: Recent Development in Turbulence Modelling. *Proceedings 3<sup>rd</sup> Symposium on Refined Flow Modelling and Turbulence Measurements*, July, 1988.
10. Pulliam, T.H.: Efficient Solution Methods for the Navier-Stokes Equations. Numerical Techniques for Viscous Flows Calculations in Turbomachinery Bladings, VKI-LS-1986-02, Von Karman Institute For Fluid Dynamics, 1986.
11. Beam, R.M.; and Warming, R.F.: Implicit Numerical Methods for the Compressible Navier-Stokes and Euler Equations. Computational Fluid Dynamics, VKI-LS-1982-04, Von Karman Institute For Fluid Dynamics, 1982.
12. Pulliam, T.H.; and Chaussee, D.S.: A Diagonal Form of an Implicit Approximate-Factorization Algorithm. *J. Comput. Phys.*, vol. 39, 1981, pp. 347-363.
13. Jameson, A.; Schmidt, W.; and Turkel, E.: Numerical Solutions of the Euler Equations by

- Finite Volume Methods Using Runge-Kutta Time-Stepping Schemes. *AIAA Paper* 81-1259, June 1981.
14. Pulliam, T.H.: Artificial Dissipation Models for the Euler Equations. *AIAA J.*, vol. 24, no. 12, 1986, pp. 1931-1940.
  15. Coakley, T.J.: Turbulence Modeling Methods for the Compressible Navier-Stokes Equations. *AIAA Paper* 83-1693, July 1983.
  16. Taylor, A.M.K.P.; Whitelaw, J.H.; and Yianneskis, M.: Developing Flow in S-Shaped Ducts, I-Square Cross-Section Duct. NASA CR-3550, 1982.
  17. Stanitz, J.D.; Osborn, W.M.; and Mizisin, J.: An Experimental Investigation of Secondary Flow in an Accelerating, Rectangular Elbow with 90° of Turning. NACA TN-3015, 1953.
  18. Chima, R.V.: Development of an Explicit Multigrid Algorithm for Quasi-Three-Dimensional Viscous Flows in Turbomachinery. NASA TM-87128, 1986.

Table I. - Grids for the Stanitz elbow

Grid number	Points	Expansion ratio
1	50x31x21	1.2
2	50x41x31	1.2
3	99x31x21	1.2
4	50x31x21	1.3
5	51x41x31	1.3

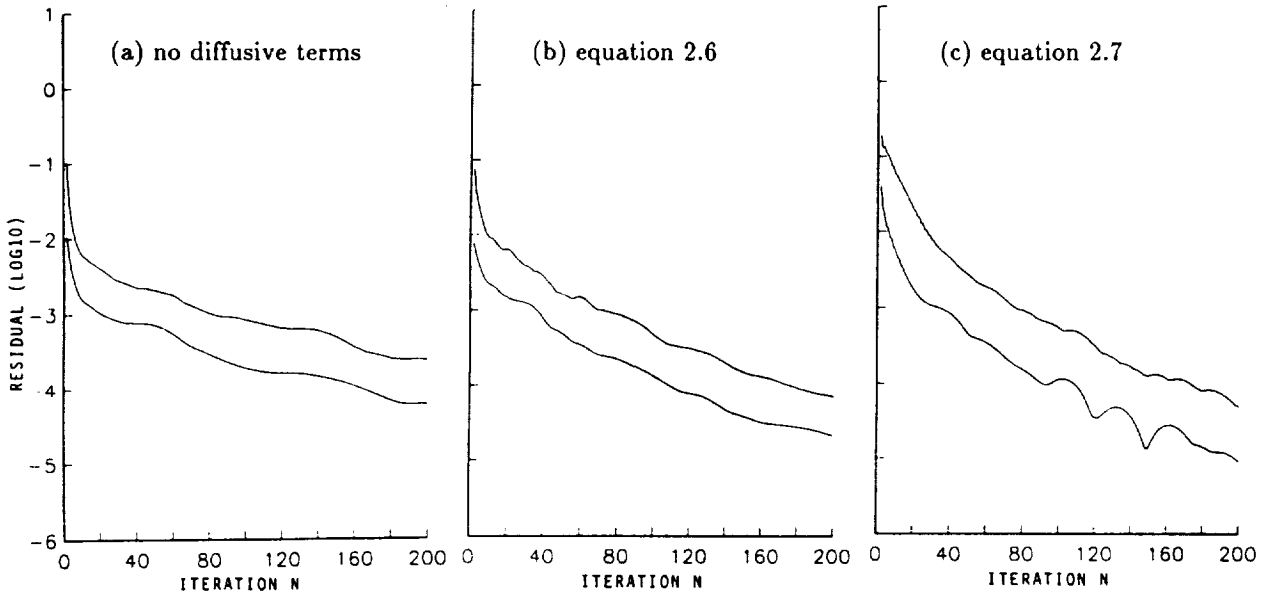


Figure 1. - Convergence tests for implicit treatment of diffusive terms.

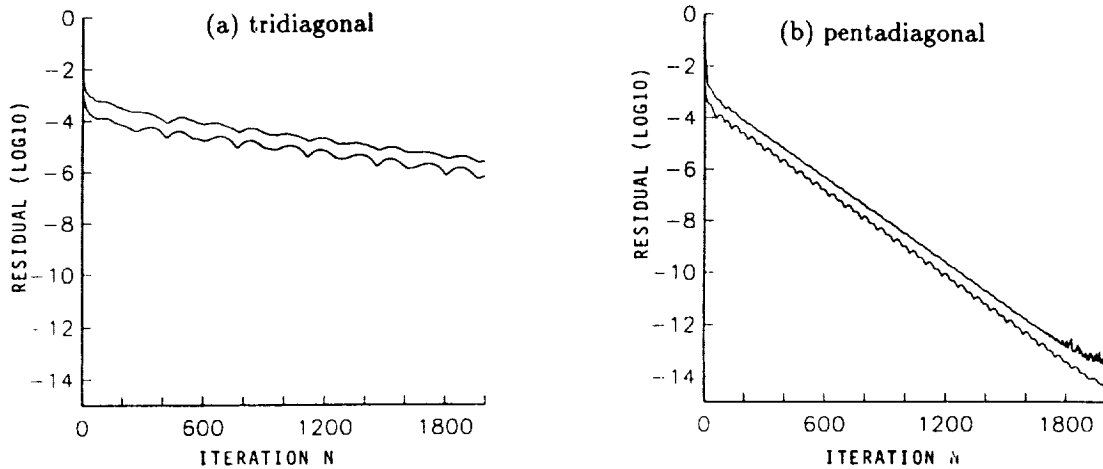


Figure 2. - Convergence tests for tri- or pentadiagonal solvers.

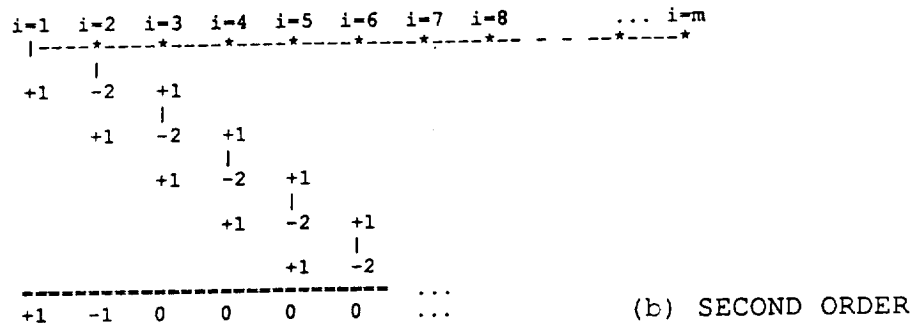
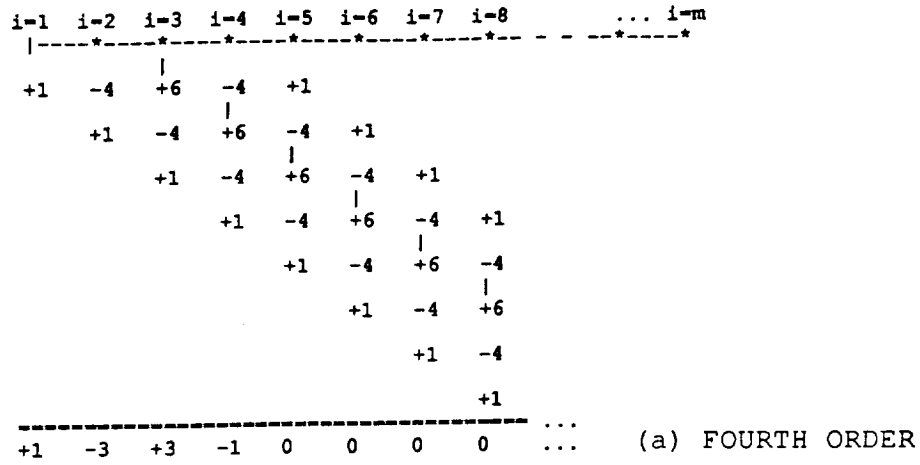


Figure 3. - Artificial dissipation treatment at boundaries.

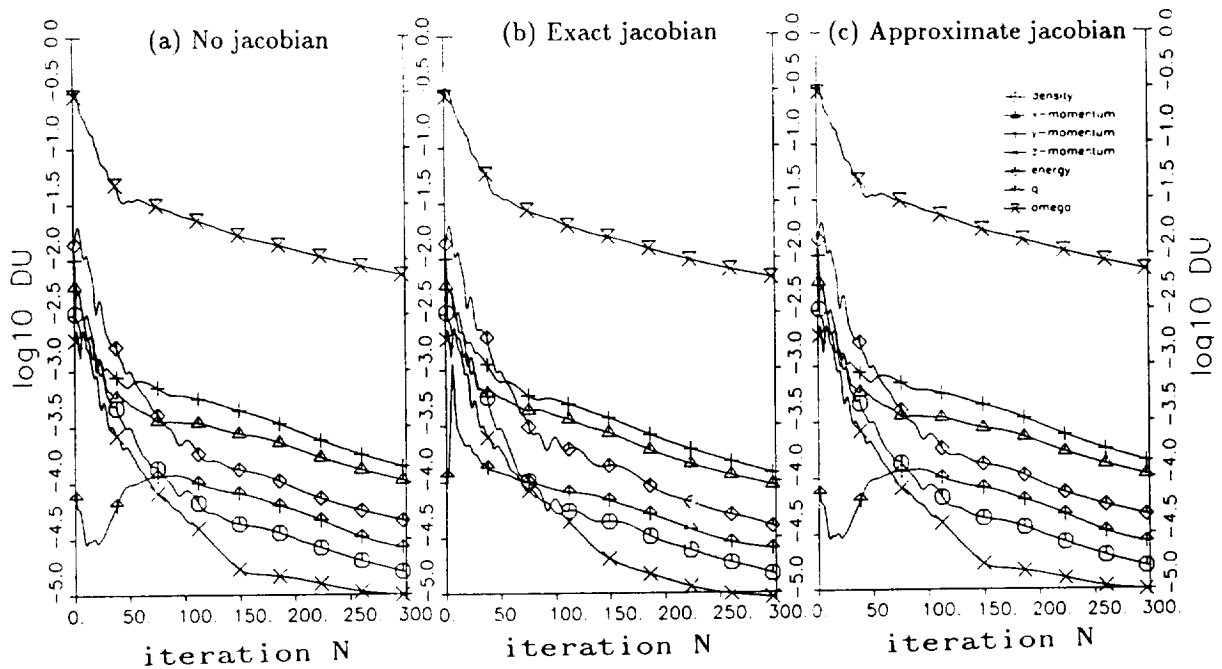


Figure 4. - Convergence tests for implicit treatment of sink-source terms.

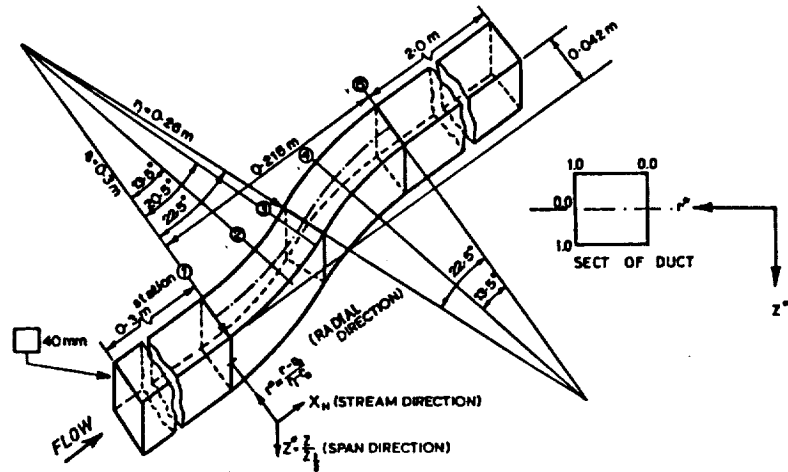


Figure 5. - Sketch of experimental setup of S-duct.

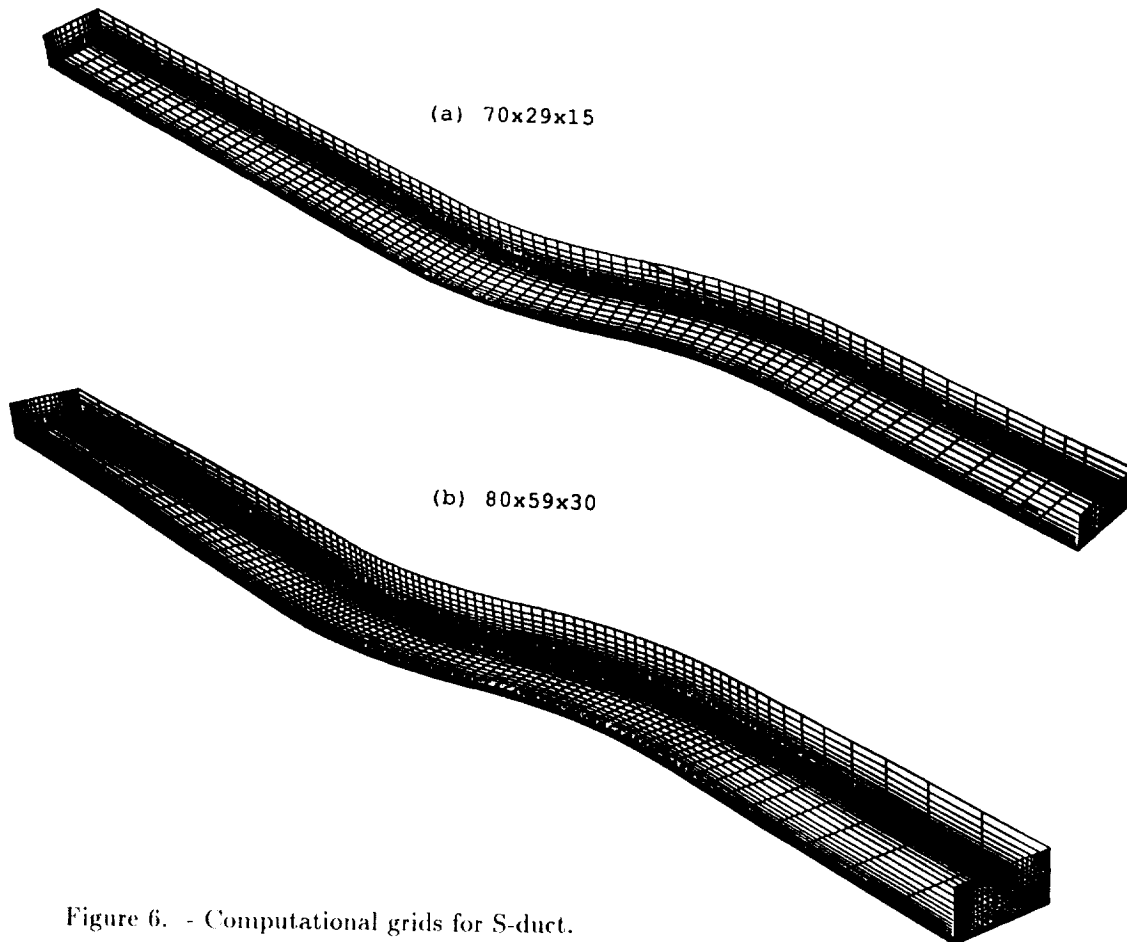


Figure 6. - Computational grids for S-duct.



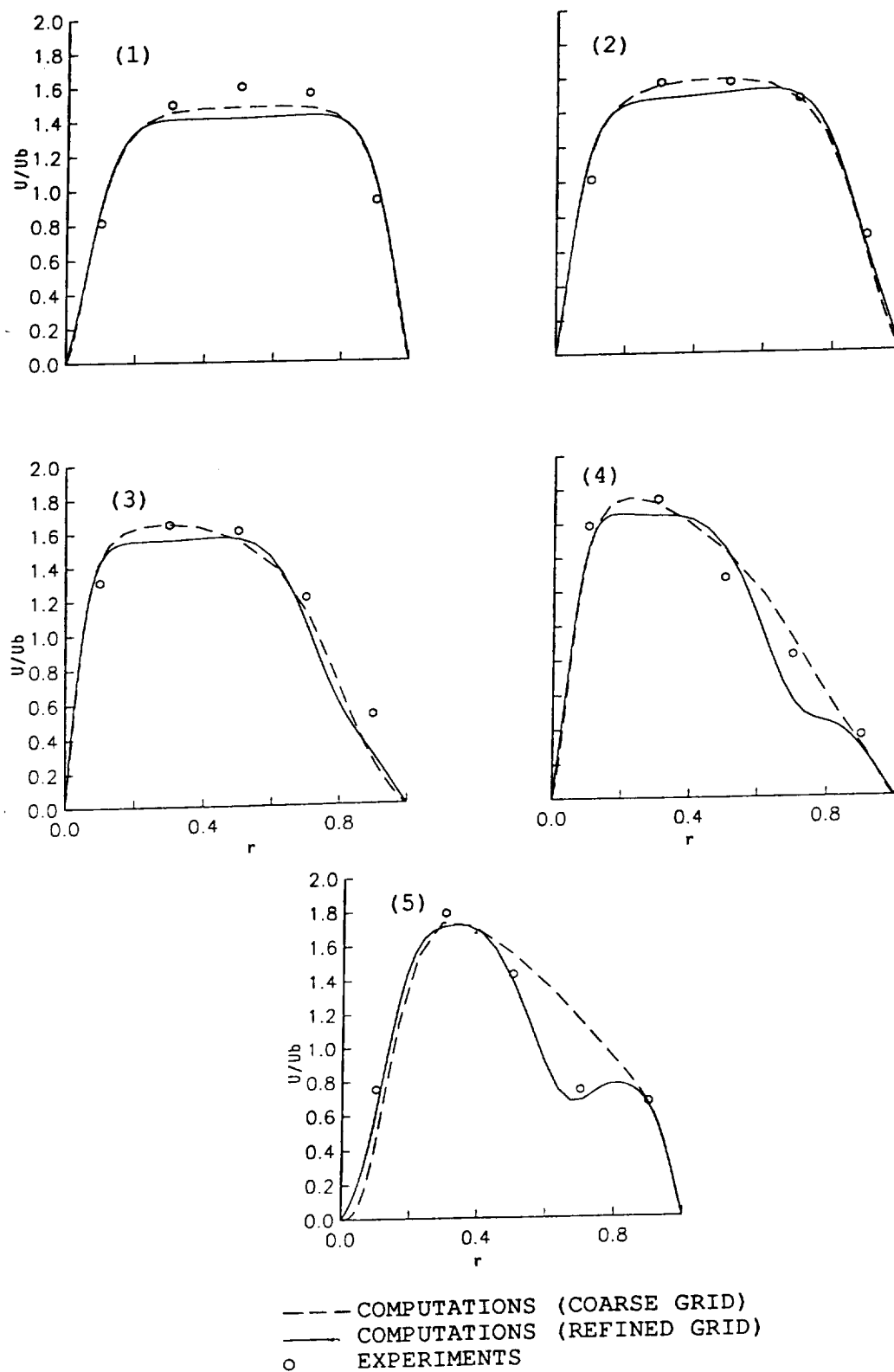


Figure 7(a). - Velocity profiles on symmetry plane of S-duct for laminar flow regime.

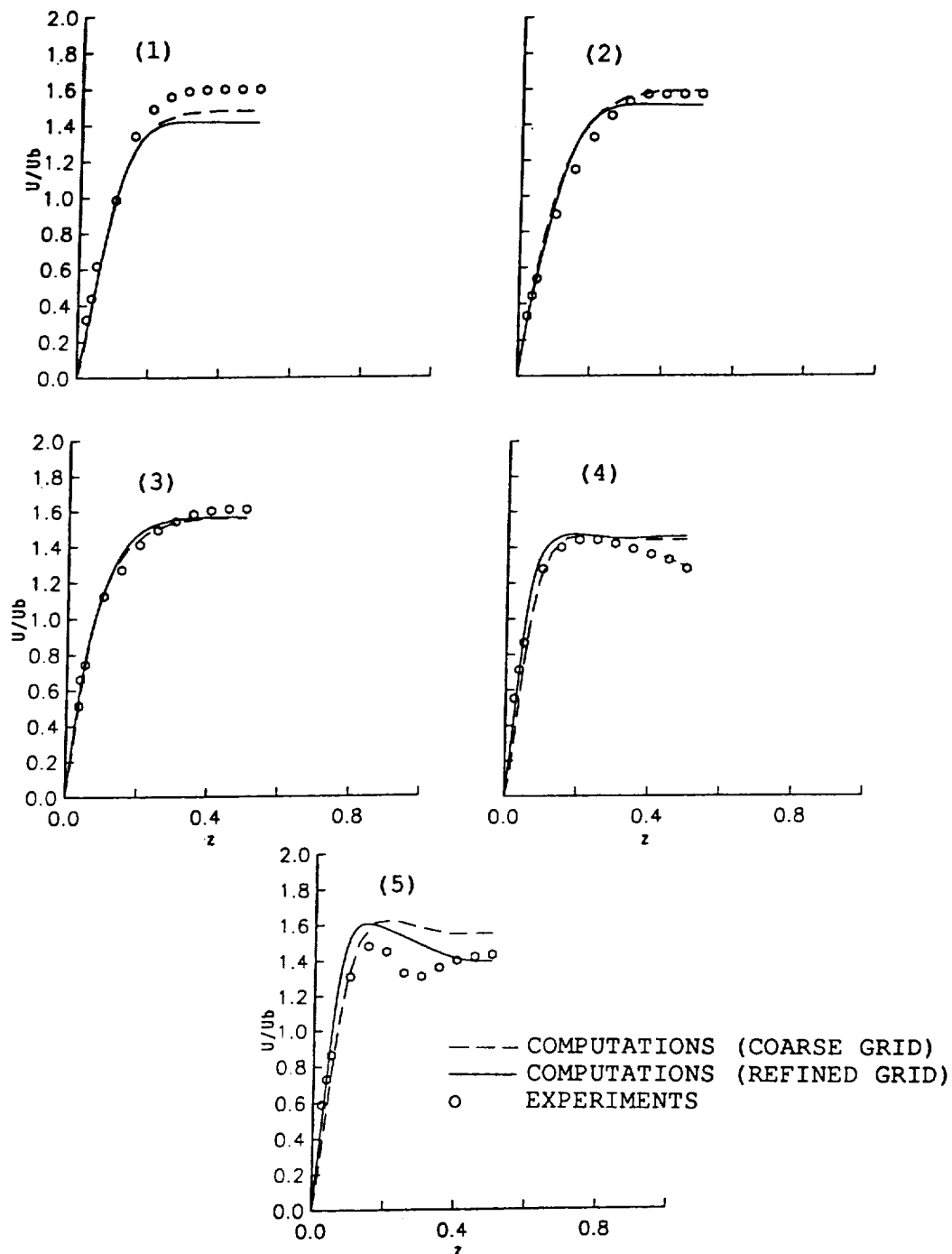


Figure 7(b). - Velocity profiles on midspan of S-duct for laminar flow regime.

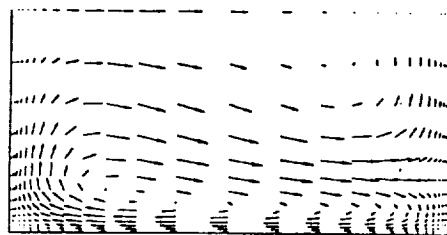


Figure 7(c). - Secondary velocity at the bend exit of S-duct for laminar flow regime.

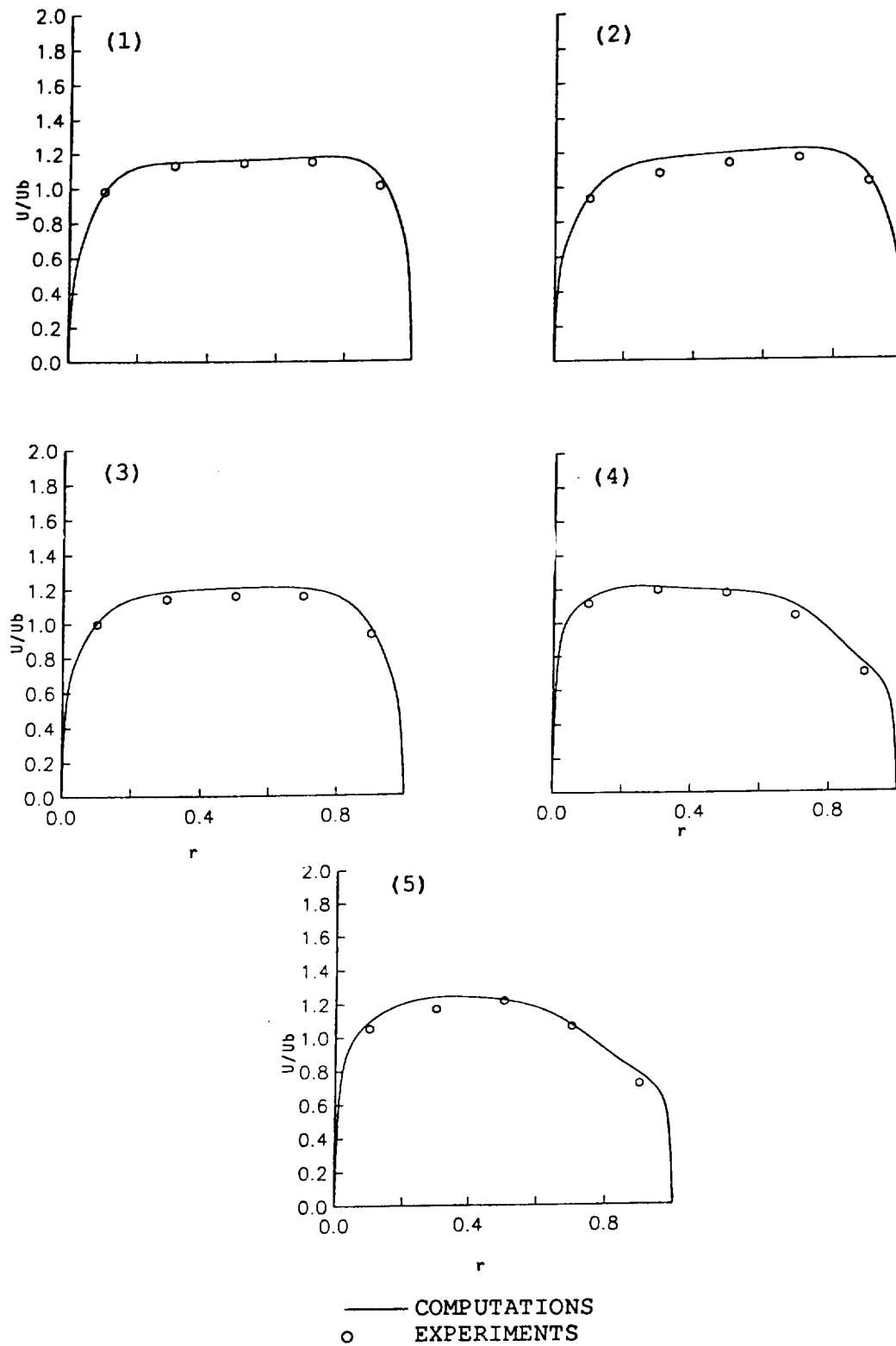


Figure 8(a). - Velocity profiles on symmetry plane of S-duct for turbulent flow regime.

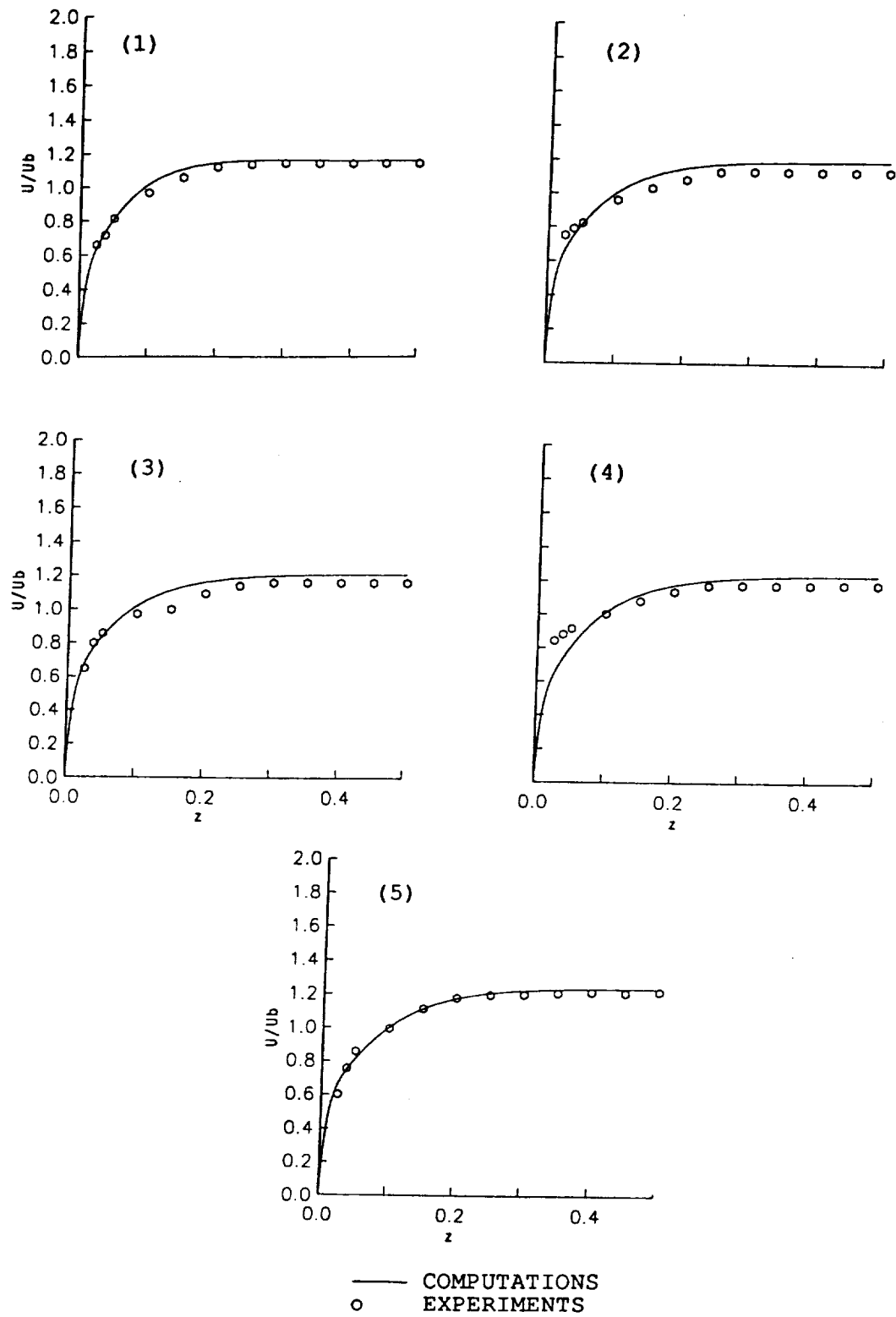


Figure 8(b). - Velocity profiles on midspan of S-duct for turbulent flow regime.

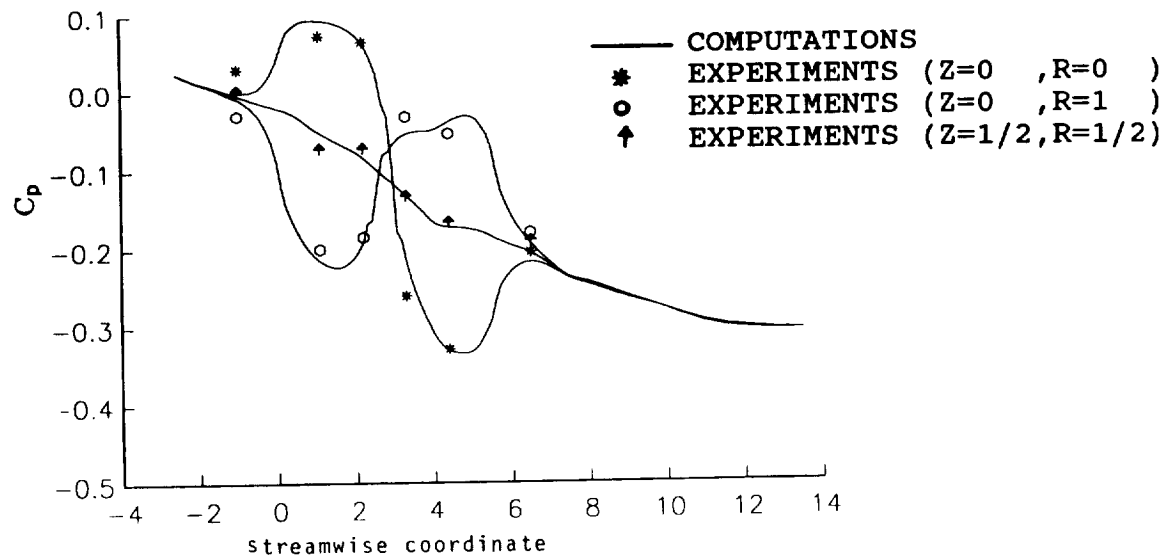


Figure 8(c). - Wall  $C_p$  distribution of S-duct for turbulent flow regime.

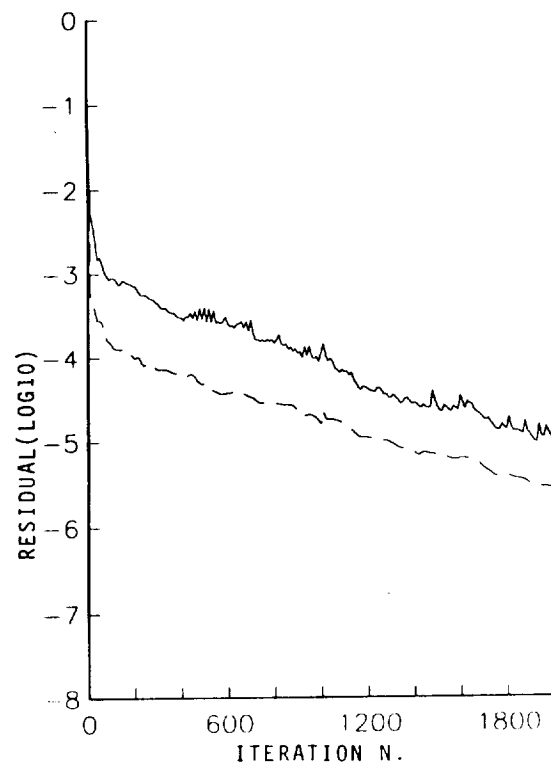


Figure 8(d). - Convergence history for turbulent flow regime.

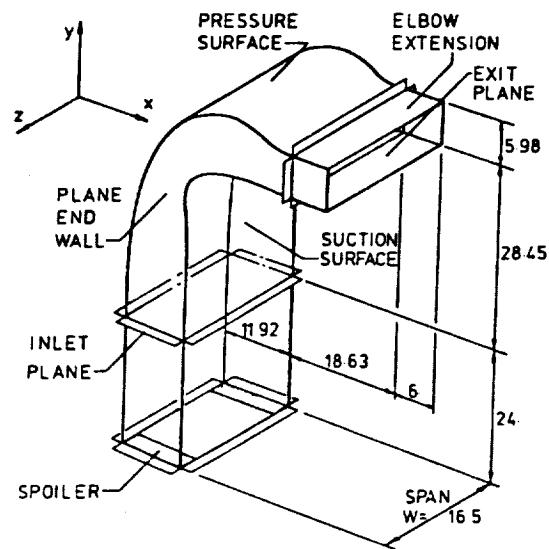


Figure 9. - Sketch of experimental setup of Stanitz elbow.

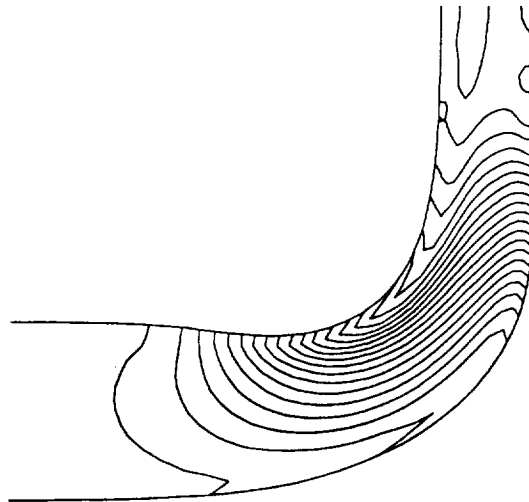


Figure 10(a). - Inviscid pressure isolines of Stanitz elbow.

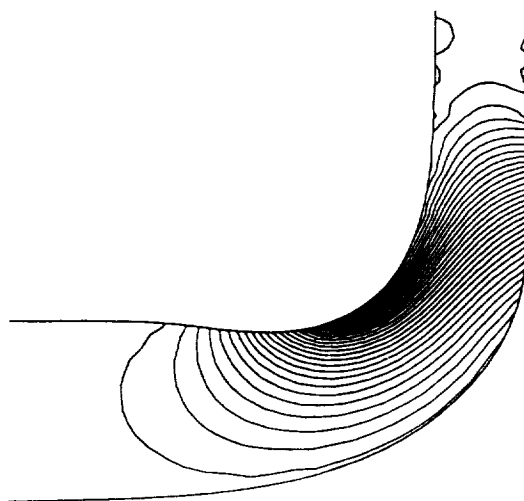


Figure 10(b). - Inviscid Mach number isolines of Stanitz elbow.

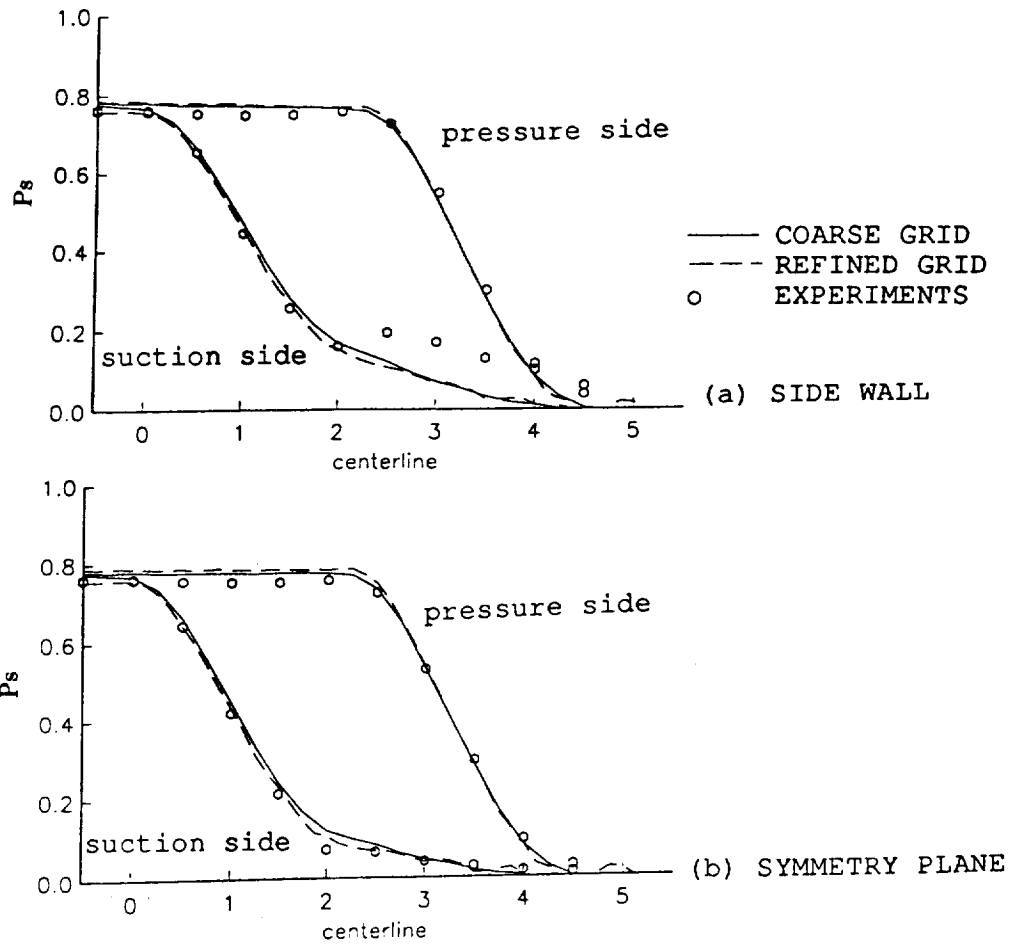


Figure 11. - Inviscid  $P_s$  distribution of Stanitz elbow.

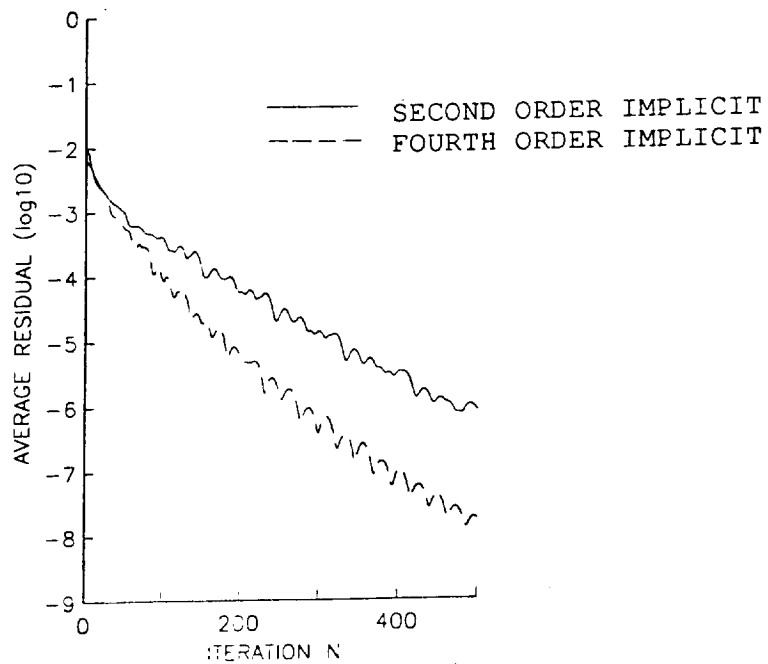


Figure 12. - Convergence history of Stanitz elbow.

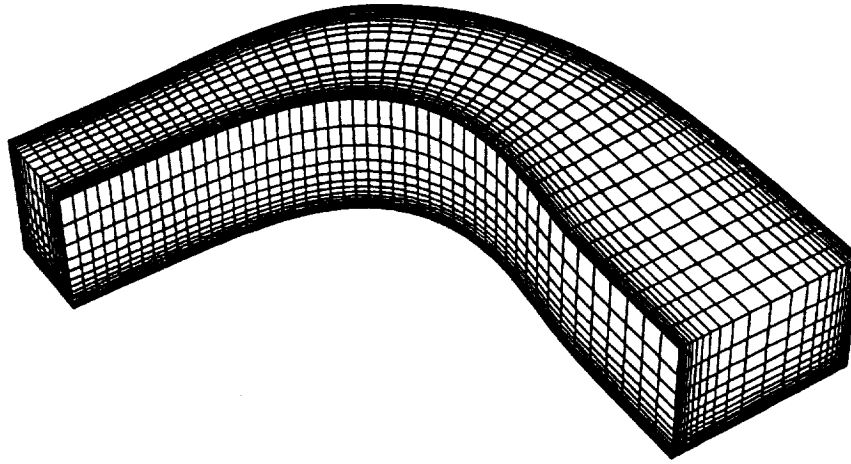


Figure 13. - Refined 50×41×31 point grid of Stanitz elbow.

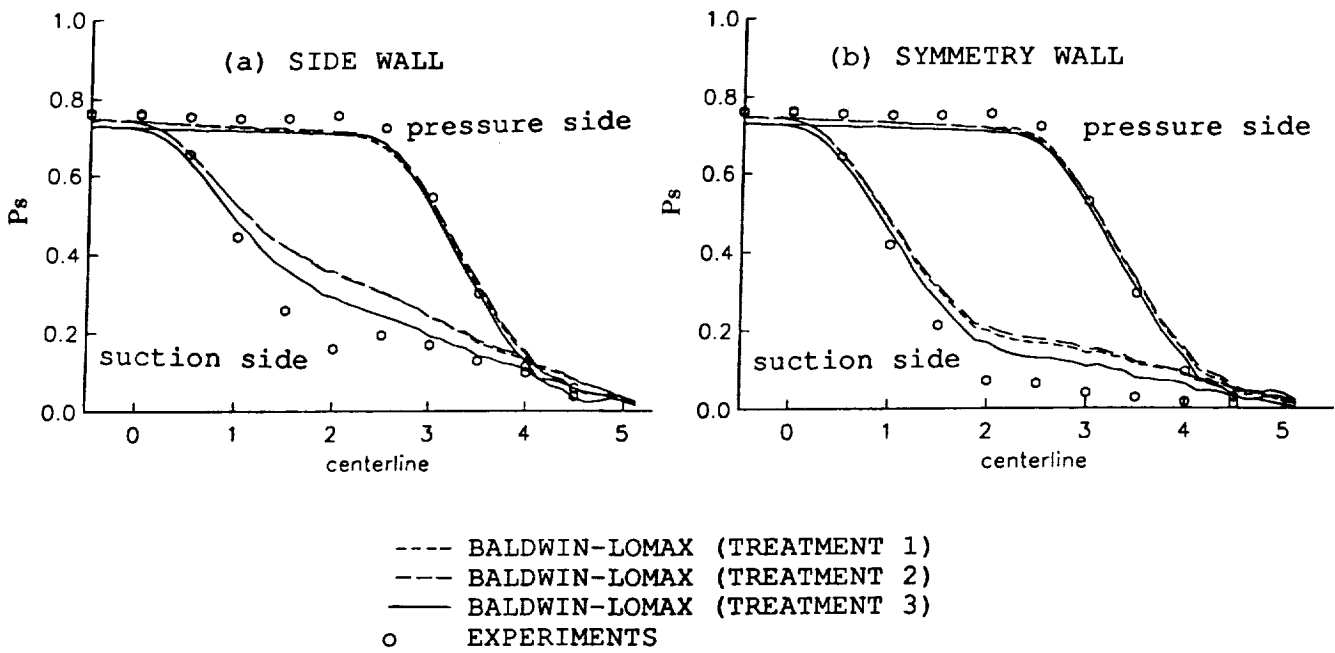


Figure 14. -  $P_s$  distribution with multiple wall treatments in Baldwin-Lomax model.



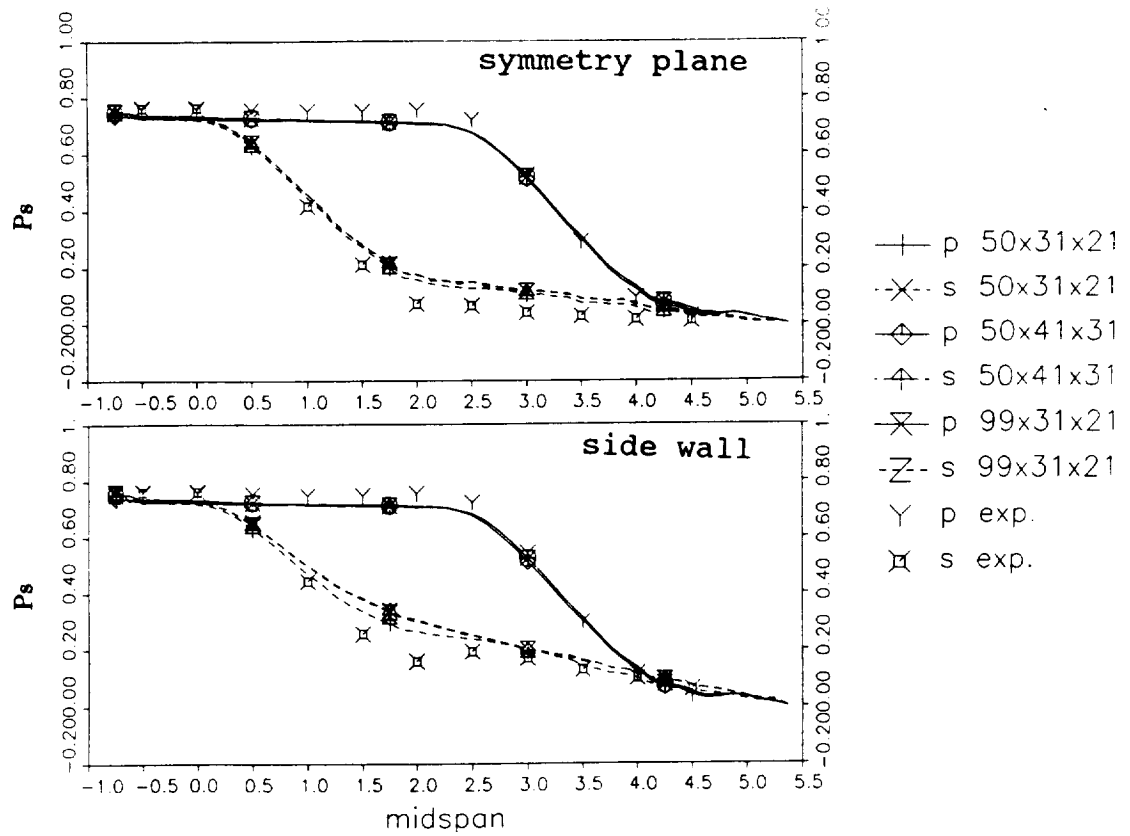


Figure 15. - Stanitz elbow.  $P_s$  dependence on grid points by Baldwin-Lomax model.

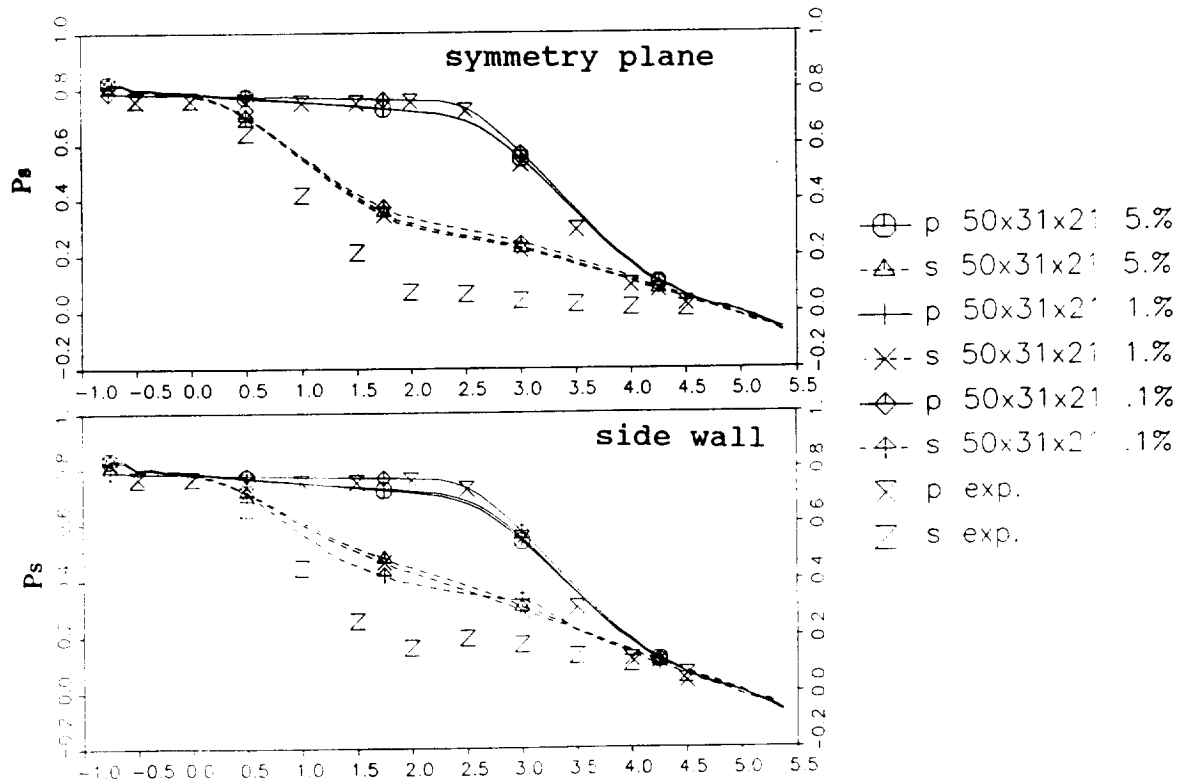


Figure 16. - Stanitz elbow.  $P_s$  dependence on turbulence level by  $q-\omega$  model (coarse grid).

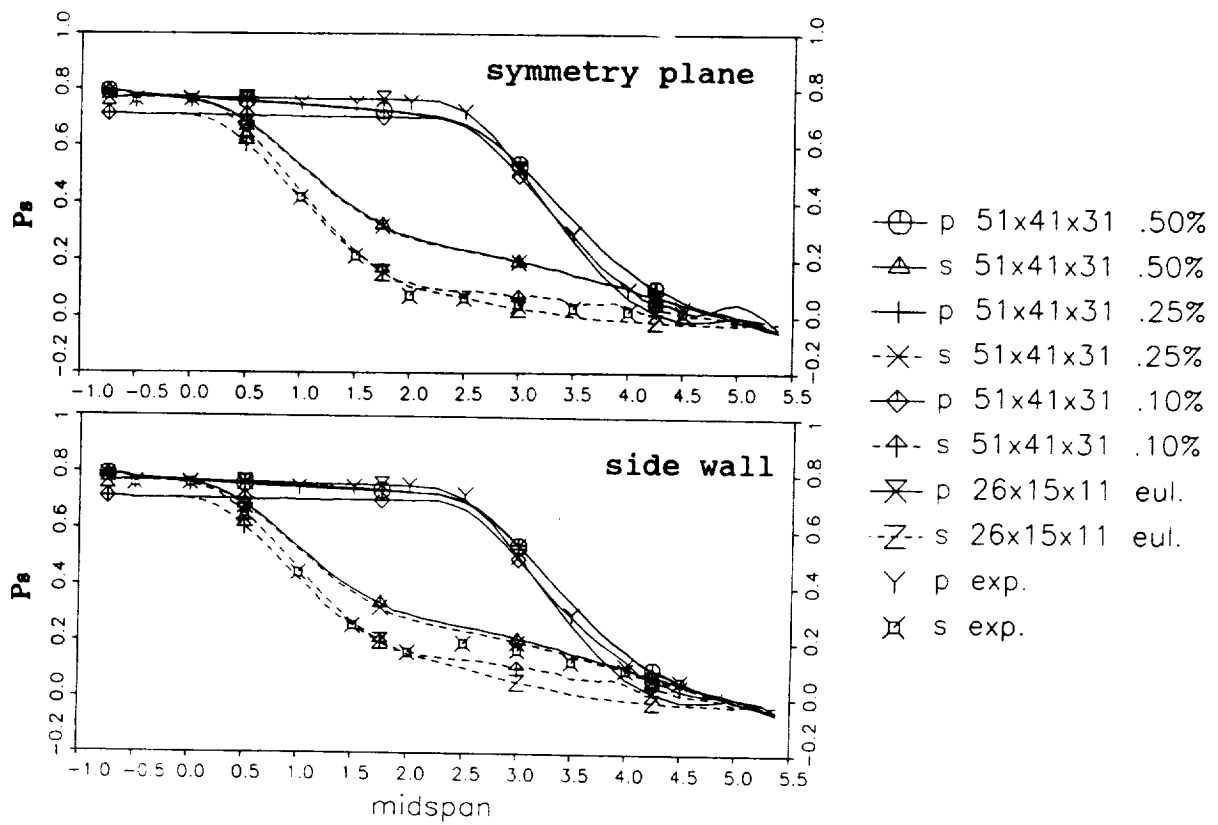


Figure 17. - Stanitz elbow.  $P_s$  dependence on turbulence level by  $q-\omega$  model (refined grid).

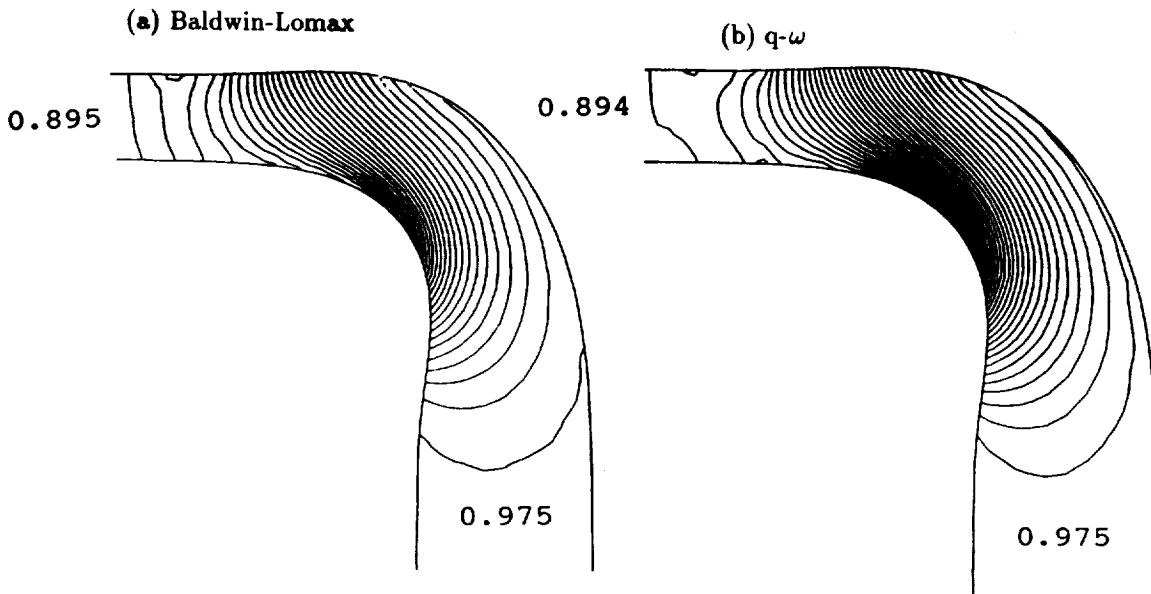


Figure 18. - Static pressure isolines on symmetry plane of Stanitz elbow.

Figure 20. - Velocity vectors at exit section of Stanitz elbow.

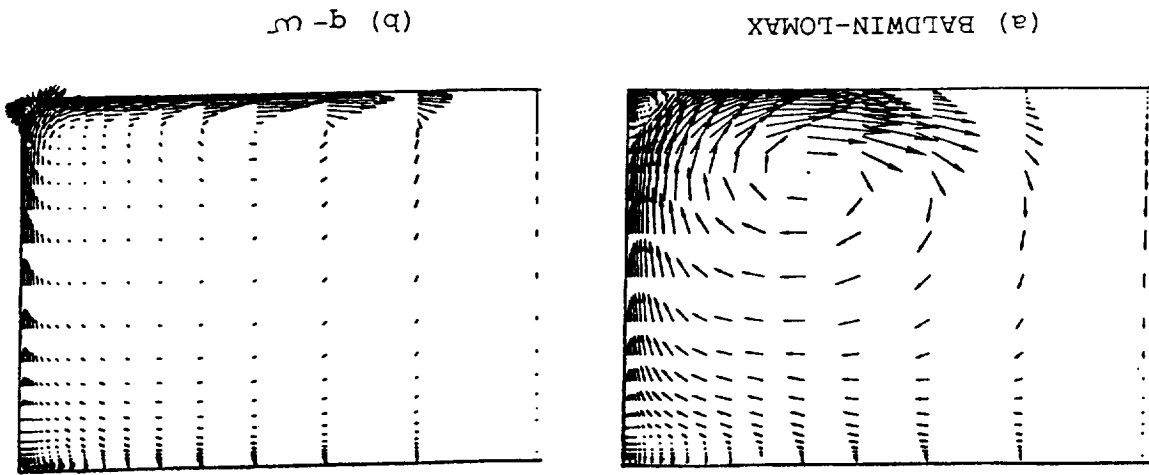
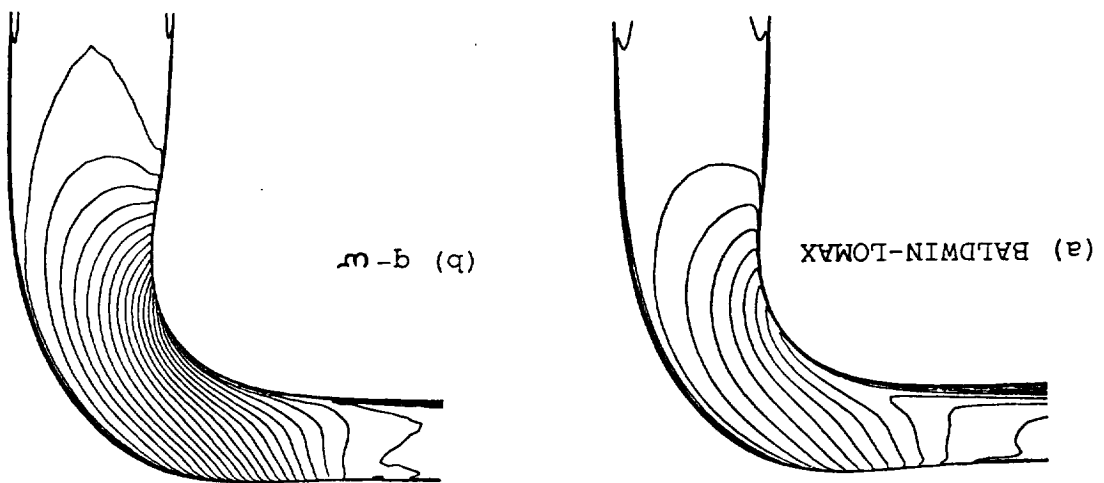


Figure 19. - Mach number isolines on symmetry plane of Stanitz elbow.



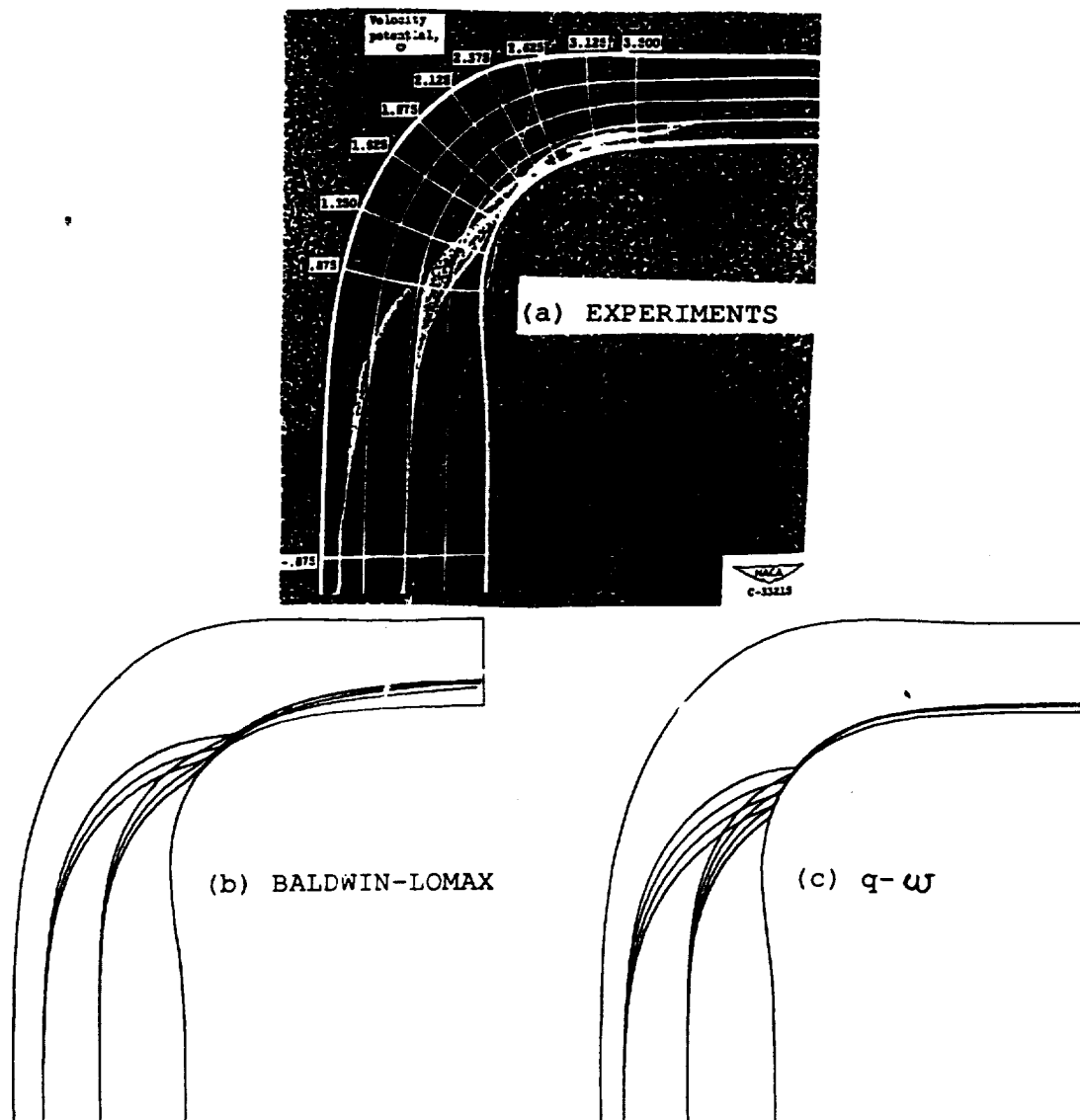
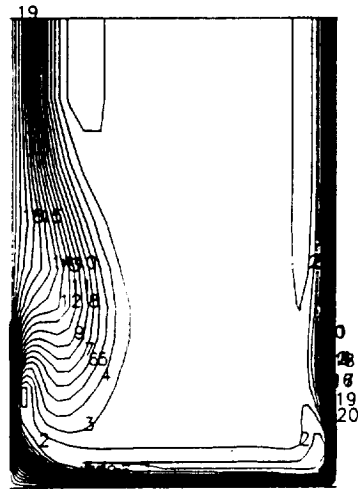
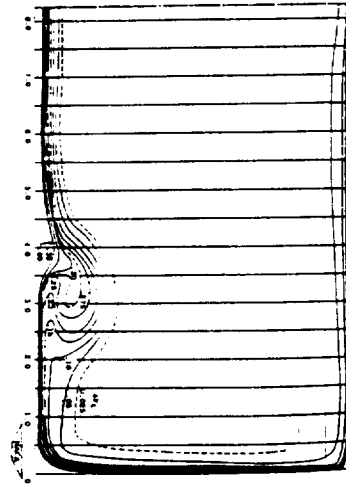


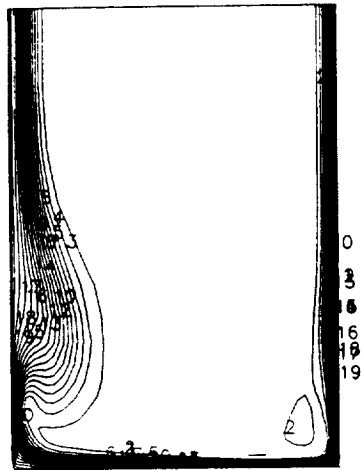
Figure 21. - Secondary flow visualization of Stanitz elbow.



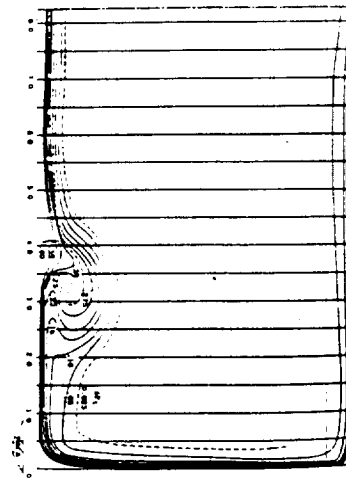
31x21 ( $r=1.2$ )



experimental



41x31 ( $r=1.2$ )



experimental

Figure 22. - Total pressure loss isolines at exit section of Stanitz elbow.

# Report Documentation Page

1. Report No. <b>NASA TM-103099</b> <b>ICOMP-90-13</b>		2. Government Accession No.		3. Recipient's Catalog No.	
4. Title and Subtitle <b>Implicit Solution of Three-Dimensional Internal Turbulent Flows</b>				5. Report Date <b>July 1990</b>	
				6. Performing Organization Code	
7. Author(s) <b>V. Michelassi, M.-S. Liou, and L.A. Povinelli</b>				8. Performing Organization Report No. <b>E-5420</b>	
				10. Work Unit No. <b>505-62-21</b>	
9. Performing Organization Name and Address <b>National Aeronautics and Space Administration Lewis Research Center Cleveland, Ohio 44135-3191</b>				11. Contract or Grant No.	
				13. Type of Report and Period Covered <b>Technical Memorandum</b>	
12. Sponsoring Agency Name and Address <b>National Aeronautics and Space Administration Washington, D.C. 20546-0001</b>				14. Sponsoring Agency Code	
15. Supplementary Notes <b>V. Michelassi, Institute for Computational Mechanics in Propulsion, NASA Lewis Research Center (work funded under Space Act Agreement C-99066-G); on leave from the University of Florence, Florence, Italy. M.-S. Liou and L.A. Povinelli, NASA Lewis Research Center.</b>					
16. Abstract <p>The scalar form of the approximate factorization method has been used to develop a new code for the solution of three-dimensional internal laminar and turbulent compressible flows. The Navier-Stokes equations in their Reynolds-averaged form are iterated in time until a steady solution is reached. Evidence is given to the implicit and explicit artificial damping schemes that proved to be particularly efficient in speeding up convergence and enhancing the algorithm robustness. A conservative treatment of these terms at domain boundaries is proposed in order to avoid undesired mass and/or momentum artificial fluxes. Turbulence effects are accounted for by the zero-equation Baldwin-Lomax turbulence model and the <math>q-\omega</math> two-equation model. For the first, an investigation on the model behavior in case of multiple boundaries is performed. The flow in a developing S-duct is then solved in the laminar regime at Reynolds number (Re) 790 and in the turbulent regime at <math>Re = 40\,000</math> using the Baldwin-Lomax model. The Stanitz elbow is then solved using an inviscid version of the same code at <math>M_{inlet} = 0.4</math>. Grid dependence and convergence rate are investigated showing that for this solver the implicit damping scheme may play a critical role for convergence characteristics. The same flow at <math>Re = 2.5 \times 10^6</math> is solved with the Baldwin-Lomax and the <math>q-\omega</math> models. Both approaches showed satisfactory agreement with experiments, although the <math>q-\omega</math> model is slightly more accurate.</p>					
17. Key Words (Suggested by Author(s)) <b>Three-dimensional flows Laminar flows Turbulent flows Reynolds-averaged Navier-Stokes equations</b>			18. Distribution Statement <b>Unclassified - Unlimited Subject Category 34</b>		
19. Security Classif. (of this report) <b>Unclassified</b>		20. Security Classif. (of this page) <b>Unclassified</b>		21. No. of pages <b>44</b>	
				22. Price* <b>A03</b>	



National Aeronautics and  
Space Administration

**Lewis Research Center**  
ICOMP (M.S. 5-3)  
Cleveland, Ohio 44135

**FOURTH CLASS MAIL**

ADDRESS CORRECTION REQUESTED



Official Business  
Penalty for Private Use \$300

Postage and Fees Paid  
National Aeronautics and  
Space Administration  
NASA 451

**NASA**

---